Interactions between deformation and dissolution-precipitation reactions in plagioclase feldspar at greenschist facies

Joe Gardner[a*], John Wheeler[a], Elisabetta Mariani[a]

[a]Department of Earth, Ocean, and Ecological Sciences, University of Liverpool, Liverpool, UK

*corresponding author: Joe Gardner (jgardner@liverpool.ac.uk)

Postal address:

Jane Herdman Building

School of Environmental Sciences

University of Liverpool

4 Brownlow Street

Liverpool

United Kingdom,

L69 3GP

Other author emails:

John Wheeler – johnwh@liverpool.ac.uk

Elisabetta Mariani – mariani@liverpool.ac.uk

Abstract

Rocks often undergo deformation and metamorphism simultaneously. However, relatively little research has been carried out on the interactions between deformation, fluid influx and a relatively-recently identified type of metamorphic reaction, termed interface-coupled dissolution-precipitation. In this study, optical microscopy and electron backscatter diffraction (EBSD) were used to investigate the interactions between deformation and dissolution-precipitation reactions in feldspar from metagabbros deformed at mid-crustal conditions. Fracturing and fluid influx promoted two types of dissolution-precipitation reactions that worked in tandem to convert Ca-bearing plagioclase to pure albite. Conventional dissolution and precipitation, here defined as dissolution precipitation reactions involving a transport step, worked to heal fractures and produce fine-grained albite. In parts of original grains that were not fractured, interface-coupled dissolution-precipitation occurred to albitize mm-cm scale grain fragments. Because interface-coupled replacement displays fast kinetics, reaction fronts were not preserved, so coupled dissolution-precipitation was identified using the following microstructural criteria: a lack of preserved zoning, indicating a fast reaction mechanism; orientation inheritance during reaction indicating epitaxial nucleation/topotactic replacement; intracrystalline strain containing Burgers vectors that indicate distortion was not derived from crystal plasticity; intragranular microporosity and second phase inclusions which share orientations with twin and cleavage planes of their parent grains. These criteria could be applied to any system to identify interface-coupled replacement in the absence of preserved reaction fronts. Brittle fracturing and dissolution-precipitation combined to result in an overall grain size reduction, and a transition from dominantly brittle to dominantly viscous deformation, producing mylonites at greenschist facies, and contributing to the development of a regional-scale shear zone.

Keywords: greenschist-facies deformation, fluid-rock interaction, dissolution-precipitation, interface-coupled replacement reactions, epitaxy, electron backscatter diffraction

1 Introduction

Fluid-rock interactions occur when aqueous solutions in the crust react with rock in an attempt to achieve thermodynamic equilibrium, involving dissolution of mineral phases that are out of equilibrium with the surrounding conditions, and precipitation of phases that are in equilibrium (Glassley, 1998). As aqueous fluids are observed throughout the crust (Bucher and Stober, 2010; Yardley and Bodnar, 2014), such interactions are a key component of crustal dynamics (e.g. Gratier et al., 2013; Jamtveit et al., 2019; Marchesini et al., 2019; Menegon et al., 2017; Menegon et al., 2008; Wintsch and Yi, 2002).

Plagioclase feldspar minerals are a major constituent of the middle to lower Earth's crust and are frequently observed in large scale crustal faults and shear zones, so knowledge of how feldspar deforms is vital to understanding the geodynamic behaviour of the crust. In addition, feldspar is an ideal mineral to study the links between deformation and fluids, because it has been shown to undergo brittle deformation, which can promote fluid influx, at most conditions within the crust (Tullis and Yund, 1992). In particular, in the middle crust, at greenschist facies conditions, feldspar displays evidence for dominantly brittle deformation (Fitz Gerald and Stünitz, 1993; Simpson, 1985; Stünitz and Fitz Gerald, 1993; Viegas et al., 2016). Microcracking is common in feldspar at all crustal conditions, due to two good cleavages on (010) and (001) (Fitz Gerald and Stünitz, 1993; Menegon et al., 2008; Menegon et al., 2013; Stünitz, 1993; Stünitz and Fitz Gerald, 1993; Stünitz et al., 2003). It is the weakest phase in gabbroic rocks, so accommodates most of the strain in those lithologies when deformed across the whole range of medium to high metamorphic grades (Brodie and Rutter, 1985). Previous work has also documented the process of reaction softening in the middle to lower crust that results from metamorphic reactions in feldspar-rich lithologies. The breakdown of feldspar can lead to the development of a two-phase mixture of either two feldspar species, such as the recrystallisation of perthite to orthoclase and Na-plagioclase (Menegon et al., 2013). Feldspar breakdown can also lead to the production of softer phases such as white mica (Gueydan et al., 2003), or result in fine-grained polyphase mixtures that are weaker than the original rocks (e.g., Stünitz & Tullis, 2001; Menegon et al., 2008; Oliot et al., 2010). These studies have shown that such reactions result in strain localisation and the development of shear zones, and therefore directly affect the strength of the crust.

Much endeavour has recently been invested in the characterisation of a recently identified type of reaction caused by the interaction between crustal fluids and rocks, termed fluid-mediated, interface-coupled replacement reactions by a number of authors (Engvik et al., 2008; Giuntoli et al., 2018; Hövelmann et al., 2009; Mukai et al., 2014; Plümper et al., 2017; Putnis, 2002; Putnis, 2009; Putnis and John, 2010; Spruzeniece et al., 2017). These reactions differ from the traditional view of dissolution of thermodynamically unstable phases and the precipitation of new, more stable phases in that, during interface-coupled replacement, dissolution and reprecipitation are coupled in space and time, i.e. dissolved product components are not transported to new sites before precipitation. Instead, dissolution and precipitation are coupled across a migrating reaction front (interface) that is lined with a nano-thin film of fluid. In such a model, the rates of dissolution of the parent phase and precipitation of the product are also coupled, but controlled by the rate of dissolution rather than nucleation, which acts to preserve the integrity of the interface (Putnis, 2009). The thin fluid film becomes supersaturated with respect to the product phase, and precipitation of the product phase occurs on the surface of the parent phase (i.e., epitaxial nucleation), preserving crystallographic orientation across the interface, and in some cases enhancing dissolution of the parent phase (Putnis, 2002). Xia et al. (2009) studied the reaction kinetics of interface-coupled dissolution-precipitation reactions in detail. Those authors showed that pseudomorphic replacement requires that precipitation must occur close to the dissolution front for nanoscale textures to be preserved, and that this is influenced by the solution chemistry of the reaction front (i.e. supersaturation with respect to reaction products), and the similarity between crystal structures, which facilitates epitaxial nucleation, therefore decreasing the activation energy of product phase nucleation. Further, Xia et al. (2009) identified three processes that could control reaction kinetics – dissolution of the reactant phase, precipitation of the product phase, and solute transport to and from the reaction front. The slowest of these processes is the rate-limiting step and so controls the overall reaction kinetics, which in turn controls how exact the pseudomorphic replacement will be. When dissolution is the rate-limiting step, coupling of dissolution and precipitation occurs over the nanoscale, leading to virtually perfect pseudomorphism, and when precipitation is rate-limiting, coupling of dissolution and precipitation occurs over the microscale, resulting in approximate pseudomorphism.

To date, relatively little research has been carried out on the interactions between deformation, fluid influx and the activation of the interface-coupled replacement process (Giuntoli et al., 2018; Mukai et al., 2014). Mukai et al. (2014) showed that fluid influx in granulite-facies anorthosites and anorthositic gabbros led to the development of amphibolite-facies shear zones containing a complex intergrowth of feldspar grains, which exhibited a crystallographic preferred orientation (CPO) developed by inheritance from interface-coupled replacement rather than crystal plastic deformation. The dominant deformation mechanism in the shear zones was diagnosed to be dissolution-precipitation creep, i.e., pressure solution. Giuntoli et al. (2018) studied the links between dissolution-precipitation and deformation in amphibolites using a combination of CL and EBSD. Their analysis indicated that fracturing and associated fluid influx promoted pseudomorphic replacement of both feldspar and amphibole grains, and encouraged deformation by dissolution-precipitation creep rather than dislocation creep in the mid to lower crust. Feldspar is also one of the main minerals in which interface-coupled reactions have been observed to occur (Engvik et al., 2014; Engvik et al., 2008; Hövelmann et al., 2009; Mukai et al., 2014; Plümper et al., 2017; Plümper and Putnis, 2009). This is due to its range of solid solution compositions that share very similar crystallographic structures (Deer et al., 2013), which can promote epitaxial growth or topotactic replacement.

This study focuses on the links between metamorphic reactions and deformation in feldspar-rich metagabbros from the Gressoney Shear Zone in the NW Italian Alps. Previous work to date has focused on mylonitized metagabbroic samples from the GSZ that have been deformed to high strain (see section 2). This work focuses on the lowest strain samples that were found in metagabbro exposures on the order of tens m^2, to investigate the processes responsible for the initiation of mylonitic textures at higher strains in the absence of crystal plastic deformation. In section 3 we describe our methods, and in section 4 we present our main observations. In section 5 we provide detailed interpretations and synthesise our arguments.

2 Geological setting

The samples analysed in this study are deformed, feldspar-rich, metagabbroic rocks from the western Sesia unit (i.e. continental crust) of the Gressoney Shear Zone (GSZ), NW Italy (Jiang et al., 2000;

Prior and Wheeler, 1999; Wheeler and Butler, 1993). No basic magmatism was recorded in the Western Alps during the Alpine Orogeny (Wheeler and Butler, 1993), and recent work on mafic plutons in the Sesia Zone used in situ dating of zircon and allanite grains to constrain the emplacement of mafic intrusions to an early Carboniferous (340.7 ± 6.8 Ma) magmatic phase (Vho et al., 2020). Extensional shear in the GSZ occurred under fluid-present greenschist facies conditions for 9 Ma, between 45 and 36 Ma (Reddy et al., 1999). Previous analysis of rocks from the GSZ has shown that albite-rich metagabbros with a mylonitic texture formed in the shear zone at greenschist facies. Prior and Wheeler (1999) showed that albite grains in the matrix of the mylonites shared a CPO. Those authors rejected crystal plastic deformation as an explanation for the development of a mylonitic fabric and a CPO, because the CPO lacked strain-related symmetry, and at the low temperatures of deformation recorded for the GSZ (< 450° C), and at natural strain rates, crystal plastic processes are understood to be insignificant in plagioclase. Jiang et al. (2000) built on the work of Prior and Wheeler (1999) to conclude that the CPOs were a product of inheritance from larger parent plagioclase clasts in the gabbro protolith, that had subsequently been modified by granular flow, defined by Stünitz (1993) as a combination of grain boundary sliding and diffusive mass transfer.

3 Methods

3.1 Field sampling

The samples used in this study were collected from a roadcut exposure of metagabbro found close to the base of the Combin Zone (UTM coordinates: 4042730 E, 5069723 N), approximately 2 km north of Estoul in the Val d'Ayas. The outcrop shows variation in strain on the sub-metre scale, with cm-wide shear bands anastomosing around less-deformed pods (tens of cm) of the same material (Fig. 1a). Samples representative of material found in the low strain pods were prepared as oriented thin sections cut perpendicular to foliation and parallel to stretching lineation (i.e. the X–Z kinematic plane), where these features could be identified (see Fig. 1b). Thin sections were cut so that their long side is parallel to the shear plane, according to field observations and oriented hand specimens, but this may be subject to slight error due to the low strain of the rocks. Deformation textures in the metagabbros were studied using polarized light and electron microscopy.

3.2 Optical microscopy

Polarized light images and whole thin section scans were collected using a Lumenera Infinity 4 camera connected to a Meiji Techno MT9000 polarized microscope, and a Leica DM2500P microscope equipped with a Leica DFC295 camera (3 mega pixel resolution) and the Leica Application Suite software. Single images collected with the Leica DFC295 camera were acquired in capture mode, and whole thin section scans were acquired as stitched images using live mode (up to 25 frames per second).

3.3 Scanning electron microscopy

Oriented thin sections were prepared for standard electron microscopy analysis and were then further polished for ~2 hours using 0.05 μm colloidal silica, to achieve the high-quality surface polish necessary for EBSD analysis. Thin sections were then cleaned, dried and carbon coated (with a thin coat of <10 nm) to ensure surface conductivity and avoid charge accumulation during analysis in the SEM.

3.3.1 BSE imaging

BSE imaging was used to analyse phase distribution and chemistry on the μm-scale. BSE images were collected on a Philips XL30 SEM with a tungsten filament in the Department of Earth Sciences at the University of Liverpool. Data were collected using an accelerating voltage of 20 kV, probe current of 6-8 nA, and a working distance of 13 ± 0.1 mm.

3.3.2 Electron backscatter diffraction (EBSD)

EBSD data were collected using a CamScan X500 CrystalProbe FEG-SEM equipped with a Nordlys F+ detector in the Department of Earth Sciences at the University of Liverpool, using a working distance of 25 mm, accelerating voltage of 20 kV, and a probe current of ~30 nA, 2 × 2 pattern binning, and step sizes which varied between 0.35 and 1.5 μm depending on grain size, so that multiple data points were collected from even the smallest grains (Humphreys, 2001; Randle, 2009; Wilkinson and Britton, 2012). EBSD data were processed using Oxford Instruments' Channel 5 software package. For data cleaning (i.e. the removal of misindexed pixels and filling of non-indexed pixels), band contrast data thresholding was used to isolate the most reliable data points, based on clarity of diffraction patterns (Hildyard et al., 2009; Prior et al., 2009), before the cleaning procedure set out in Prior et al. (2002) and Bestmann and Prior (2003) was followed. Missing data points were filled from nearest neighbours, and single misindexed pixels within grains were removed. A 180° systematic misindexing error about the [201] axis, which is common to feldspar due to monoclinic pseudosymmetry, was also removed using the inbuilt Channel 5 routine. Pole figures were plotted using Oxford Instruments' Channel 5 software, using a 180° rotation around the z-axis, to bring the SEM and EBSD image reference frames into coincidence. Both upper and lower hemispheres were plotted because, in triclinic feldspar, opposite crystallographic directions (e.g. [100] and [$\bar{1}$00]) are not symmetrically equivalent.

3.4 Weighted Burgers Vector method

The Weighted Burgers Vector (WBV) is a quantity calculated from orientation gradients measured within deformed crystals by EBSD. The WBV uses misorientations between pixels in EBSD maps to calculate the density of dislocation lines, summed over all dislocation types and multiplied by their Burgers vectors, that intersect with an EBSD map plane. The resultant value assigned to each pixel of the EBSD map is a vector quantity, whose magnitude defines a lower bound magnitude of the dislocation density tensor, and whose direction is a weighted sum of the Burgers vectors of geometrically necessary dislocations present in the microstructure (Wheeler et al., 2009). The WBV is calculated from EBSD data using the CrystalScape software developed by John Wheeler at the University of Liverpool (Wheeler et al., 2009).

4 Results

4.1 Observations of textures and structures in whole thin sections

The metagabbros contain mm-scale grains of albite that are surrounded by matrix grains of identical composition with a grain size on the order of tens of μm diameter (Fig. 1). The metagabbros also contain large (mm- to cm-scale) clinopyroxene porphyroclasts that show abundant evidence for brittle behaviour (commonly fracturing along cleavage planes), and are sometimes altered to minor hornblende (Fig. 1b–d). Small albite grains with equilibrium 'foam texture' can locally be observed to fill fractures in the clinopyroxene grains. Fractures can be tracked across multiple large grains of both pyroxene and feldspar, indicating all phases present in the original gabbro underwent some degree of brittle fracture (Fig. 1e–f). The hornblende has previously been interpreted as late magmatic, and because basic magmatism was never recorded in this region of the Alpine orogeny, and the hornblende shows poor preferential alignment, it is therefore likely to predate deformation and be of pre-Alpine origin (Wheeler and Butler, 1993). In contrast, both the clinopyroxene and hornblende porphyroclasts are overgrown by actinolite, which is observed predominantly in higher strain samples than those presented here, where it is aligned parallel to the bulk rock foliation (see Prior and Wheeler, 1999). Minor chlorite rims (tens of µm thickness) grow along fractures and cleavage planes. Neither clinopyroxene or hornblende occur as fine grains. Clinozoisite often occurs in bands or clusters that lie between the clinopyroxene porphyroclasts and the large albite grains and fine-grained albitic matrix. Chlorite most commonly occurs in irregular fractures and along cleavage planes within the clinopyroxene. Fracture patterns on the thin section scale follow the geometrical relationship commonly observed in fault rocks, and described in fault gouges by Rutter et al. (1986) and Logan et al. (1992). R_1 and R_2 Riedel shear bands, P foliations, and Y and X fracture arrays can be observed in all samples analysed in this study (Fig. 1e–f). Cracking along cleavage planes can also be observed, and is most evident in clinopyroxene porphyroclasts (Fig. 1b–d). Hydrous secondary phases, in particular clinozoisite, can sometimes be observed to grow along cleavage planes in albite, indicating fluid infiltration occurred along those planes (see Fig. 2b).

The metamorphic assemblage indicates that the rocks never experienced conditions higher than greenschist facies. This result is in line with previous findings, which indicate that the metagabbros experienced a single phase of metamorphism and deformation in the greenschist facies (Prior and Wheeler, 1999; Wheeler and Butler, 1993).

FIGURE 1 HERE

4.2 Large albite grains

The large albite grains exhibit faint undulose extinction, and subgrains can be observed in places. Large grains are commonly cross-cut by bands of small grains (Fig. 2a; see section 4.3 for a full discussion of small grains in the samples). These fine-grained bands are oriented parallel to preserved fractures in adjacent clinopyroxene grains. There is no difference in composition between the large grains and the fine-grained bands that cross-cut them, and the large grains show no evidence for any chemical zoning (Fig. 3). These results are in agreement with previous microprobe analysis of albite grains in higher strain samples from the GSZ (Prior and Wheeler, 1999).

FIGURE 2 HERE

The large albite grains contain abundant inclusions of reaction products common to greenschist facies metamorphism (clinozoisite, actinolite, and chlorite). The position and orientation of some inclusions appears to be crystallographically controlled, while others are distributed more randomly. In particular, clinozoisite, can often be observed to have grown elongate parallel to twin planes (Fig. 2b, black arrows). In parts of the large albite grain cores, microporosity can sometimes be observed (Fig. 2b–c), and small (a few μm diameter) secondary phase product inclusions are often present (Fig. 2c). Microporosity and small inclusions are mainly present in regions of the large grains that lack twinning or obvious evidence for fracturing (e.g. white arrow in Fig. 2b denotes area between twins).

Figure 2d shows an albite grain that has largely been protected from deformation by inclusion in a large clinopyroxene grain. The clinopyroxene grain exhibits multiple fractures, one of which cross-cuts the bottom end of the feldspathic inclusion, again indicating that fracturing crossed phase boundaries. Within the clinopyroxene, the fracture is filled with fine-grained clinopyroxene and chlorite, and fine-grained albite is present in association with the feldspar grain. The albite inclusion is itself littered with inclusions of clinozoisite and actinolite. The interface between the albitic inclusion and the clinopyroxene is lined with an actinolite reaction rim (see Fig. 7a for an EBSD derived phase map).

FIGURE 3 HERE

EBSD maps of the large albite grains reveal the presence of lattice distortions within those grains. Figure 4a shows an EBSD map (IPF-X colour scheme) of part of the grain presented in Fig. 2a, which contains both a wide band (named band A) and a fine band (band B) of small grains. In both types of band, the small grains are primarily bordered by high-angle grain boundaries (fuchsia > 15° misorientation). In the core of the large grain, a network of low angle boundaries can be observed (yellow > 2°, lime green > 5°, blue > 10°). Orange boundaries show the distribution of pericline twinning (a 180° rotation about the [010] twin axis, with a composition plane subparallel to the (001) plane) within the large and small grain populations. Distinct subgrains are occasionally observable in the large albite grain, but, more commonly, subgrain walls occur as a distributed network that is ubiquitous in all analysed large albite grains and grain fragments.

Lattice distortion in the small and large albite grains can be quantified by applying the Weighted Burgers Vector (WBV) algorithm to EBSD data (Wheeler et al., 2009). WBV magnitudes calculated over the map area are large in the large grain, indicating intragranular distortion (Fig. 4b). Such distortion is ubiquitous in all large albite grains that were analysed in the low strain GSZ metagabbro samples. In contrast, WBV magnitudes calculated for the small grains in both band A and band B are small, indicating they lack the intragranular distortion that characterises the large grains. Similar analyses of other samples show this to be the case in all small grains in the low strain samples.

FIGURE 4 HERE

Figure 5 shows pole figures constructed using data from (a) the bulk crystal, (b) band A, and (c) band B (see section S1 of the supplementary material for exact regions of map). Upper and lower hemispheres are plotted to account for the triclinic symmetry of albite. The data are plotted using the Euler map colours (top row of pole figures in Fig. 5) and with contouring (bottom row in Fig. 5). The albite grain plots as essentially a single crystal on a pole figure, although the intracrystalline distortion creates a spread of a few degrees in the distribution (Fig. 5a). The pole figures show that the grain is oriented so that the (010) plane lies subparallel to the plane of the EBSD map (see also section S2 of the supplementary material for a low albite crystal diagram drawn in the same orientation as the large grain). The pole figures constructed from small grain data show spread around the same orientation, indicating the small grains share a close orientation relationship with the large grain. The pole figures for the bands of small grains are further described in section 4.3.

FIGURE 5 HERE

All analysed large grains in the low-strain GSZ metagabbros showed evidence of intense intracrystalline distortion. Figure 6a shows an EBSD map taken from the core of an albite grain (fuchsia box in Fig. 2a), which records misorientation, in degrees, calculated relative to the white star in the centre of the image. Relative misorientation is of consistently low magnitude, in general under 5°, and locally predominantly under 2°. Intracrystalline distortion recorded by EBSD can be described in terms of geometrically necessary dislocations, or GNDs; i.e. the dislocation population required to be present to account for the measured lattice curvature (Nye, 1953). An advantage of the WBV method is that possible Burgers vectors of the GND population of a distorted crystal can be constrained with minimal assumptions (Wheeler et al., 2009). Figure 6b presents an EBSD band contrast map from the core of the large albite grain (fuchsia box in Fig. 2a), overlain with the crystallographic directions calculated for the WBV at each pixel, for all pixels with a WBV magnitude greater than 0.015 μm^{-1}. The shortest WBVs in any dataset are prone to the highest angular errors (Wheeler et al., 2009). The WBV software generates a histogram of WBV lengths, which always contains a peak at low values. This peak represents noise in the data, so only WBVs with lengths greater than those within the peak should be considered robust. A minimum WBV magnitude value of 0.015 μm^{-1} was used for the plot in Figure 6b, so as to omit the shortest, most error-prone WBVs.

Pixels in Figure 6b have been coloured with respect to crystallographic directions using the IPF colour scheme. The map shows a range of pixel colours, i.e. WBV orientations. Some of the coloured pixels are arranged in rows, which highlight subgrain wall traces oriented WNW-ESE and NNE-SSW. These traces are subparallel to the traces of the poor, {110}, and perfect, {001}, cleavage planes of the grain, respectively (see also crystal diagram in section S2). Section S2 of the supplementary material shows a close up of part of the map where the <010> Burgers vector clearly dominates the dislocation population, as well as other regions of the map where other Burgers vectors such as <001> are prominent. In these zoomed regions, <010> and <100> WBVs tend to be associated with WNW-ESE subgrain wall traces, while <001> WBVs are commonly associated with NNE-SSW traces. Notably, blue in the IPF colour scheme indicates the presence of Burgers vectors with a <010> crystallographic direction (see IPF key, Fig. 6b inset), which has never been identified as a slip direction in plastically deformed feldspar (Kruse et al., 2001; Stünitz et al., 2003). Section S2 of the supplementary material shows a close up of part of the map where the <010> Burgers vector clearly dominates the dislocation population, as well as other regions of the map where other Burgers vectors such as <001> are prominent.

FIGURE 6 HERE

Figure 7 shows EBSD data from a twinned feldspar grain that was largely protected from brittle deformation by inclusion within a large clinopyroxene grain, as presented in Figure 2d. As the protolith of this rock was a gabbro, the original feldspathic inclusion must have been Ca bearing, and as it now lacks detectable Ca (see section S3 of the supplementary material), it must have undergone a metamorphic transition to pure Ab. The original grain was twinned, and the twin pattern has been preserved during its transition to albite (Fig. 7b–c), recording that the lattice orientation of the original grain was also preserved during replacement. The preservation of this pattern indicates that replacement to albite was approximately pseudomorphic (see section S4 of the supplementary material for further analysis of the twin pattern). The twinned albite grain exhibits a similar pattern of intragranular lattice distortion to the grain shown in Figure 4. An actinolite reaction rim has developed at the original plagioclase–clinopyroxene boundary. Clinozoisite grains have grown throughout the new albite grain, growing aligned to, and in places inheriting, the original twin plane (white arrow in Fig. 7b). The albite grain has a ‘tail’ consisting of fine-grained albite where the original plagioclase grain was cross-cut by a fracture in the clinopyroxene. The fine-grained albite tail is discussed in detail in section 4.3.

FIGURE 7 HERE

4.3 Small grains

Bands of fine-grained albite, of about the same size as matrix albite, can be observed to cross-cut some of the large albite grains (e.g. Fig. 4). The composition of the large and small grains is the same, at An0 (Fig. 3).

A relatively wide (300–400 µm) band of small grains, designated band A, can be seen to run through the centre of the large albite grain presented in Figure 4. Band A contains small grains with a mean diameter of ~40 μm (see section S5 of the supplementary material for a grain size distribution histogram and related statistics). In this band, grains are predominantly equant (i.e. have aspect ratios close to one), and typically exhibit lobate boundaries and 120° triple junctions.

A smaller (50–70 μm-wide) band, designated band B, runs from the centre-left of the larger band, then turns towards the top left corner of Figure 4. These grains exhibit the same texture as those in band A, but have a smaller grain size, with a mean diameter of ~21 μm (see section S5 of the supplementary material for a grain size distribution histogram and related statistics). Both bands of grains are characterised by high-angle boundaries (> 15°, coloured fuchsia). The small grains in the tail of the protected albite grain in Figure 7 show similar microstructural characteristics as the small grains in bands A and B in Figure 4, displaying mostly high-angle lobate boundaries and 120° triple junctions.

The orientations of the traces of the bands of small grains in Figure 4 are not associated with common cleavage planes in feldspar. The large grain is oriented such that the (010) plane is parallel to the plane of the map, and the (001) plane runs approximately NNE–SSW, at a high angle to the map plane (see pole figures in Fig. 5). However, band A and part of band B are sub-parallel, and oriented so that they may originally have been related to R_2 fractures associated with right-lateral shear deformation, and the bands that run at an angle of ~90° to the main bands may be associated with P-foliation traces (compare with red box in Fig. 1c and e; Logan et al., 1992).

Figure 4b displays the WBV magnitude for the large albite grain and the bands of small grains. The WBV can be taken as a proxy for dislocation density (note that units for dislocation density and WBV are different; see Wheeler et al. (2009) for details). The large grain displays relatively high WBV magnitudes, indicating lattice distortion, whereas both bands of small grains consistently yield WBV magnitudes << 0.01 μm^{-1}, indicating they are nominally strain free. The small grains in the ‘tail’ of the albite grain in Figure 7 similarly lack evidence of intragranular distortion.

Pole figures constructed from a) the large albite grain, b) band B and c) band A in Figure 4 show the smaller grains broadly share an orientation relationship with the large grain (Fig. 5). The clusters of each of the principal crystallographic directions plot in the same quadrant and hemisphere in each set of pole figures (note that triclinic minerals do not share symmetry across hemispheres). The large grain (Fig. 5a) shows a single crystal distribution. Small grains in band B (Fig. 5b) show a spread in orientations away from the large grain orientation, particularly in the [100] and [010] plots. Grains in the wider band A (Fig. 5c) show greater dispersion of the clusters in the plots of all three crystallographic directions, but the overall orientation relationship is maintained. The patterns of dispersion in the orientations of fine grains in bands A and B occur around an axis close to the centre of the pole figure. Such dispersion paths have been observed in previous studies (e.g., Bestmann and Prior, 2003; Menegon et al., 2013), and are interpreted to be derived from rigid body grain rotations which record the bulk vorticity axis of shear zones, when constructed from oriented samples.

The twin orientations that occur in the large grains in Figures 4 and 7b can also be seen in the small grain populations in both datasets. Grains with twin orientations (180° rotation about the (010) axis, and subparallel to the (001) plane, following the pericline twin law) can be identified by their very high-angle misorientations with respect to neighbour grains (orange boundaries indicate misorientation > 170°). In Figure 7a, the blue and green colours characteristic of twin segments in the unfractured grain are also present in the tail of small grains. The fact that twin orientation relationships are shared between large grains and the small grains further suggests the orientation of the small grains has been inherited from the large grains.

5 Discussion

5.1 Initial fracturing in the GSZ metagabbros

Evidence from nature and experiments points to the fact that (micro)fracturing is the dominant deformation mode in coarse-grained feldspar at greenschist facies conditions in the Earth’s crust (Kruse et al., 2001; Menegon et al., 2008; Menegon et al., 2013; Stünitz, 1993; Stünitz and Fitz Gerald, 1993; Tullis et al., 1990; Tullis and Yund, 1987; Viegas et al., 2016). At the thin-section scale, multiple features show that the low strain GSZ metagabbros underwent brittle deformation during shear. Clinopyroxene grains exhibit cleavage fractures and other fracture offsets (Fig. 1). Fracture traces can be tracked across clinopyroxene-albite phase boundaries (Figs. 1c–d, 2d, 7).

Fractures traced on the thin section scale are shown to be in orientations consistent with those outlined by Rutter et al. (1986) and Logan et al. (1992). Hydrous, greenschist-facies second phases ubiquitously litter the interiors of the large albite grains. Second phases are commonly aligned (sub)parallel to twin/cleavage planes in the large albite grains, where twinning patterns are present (Figs. 2b and 7), indicating microfracturing and fluid infiltration occurred on these planes. Fine-grained bands of albite (Fig. 4), and the tail of albite grains presented in Figure 7, can be correlated with fracture traces in neighbouring clinopyroxene. Taken together, these features indicate that the fine-grained bands that cross-cut the large albite grains represent healed fractures. Initial fracturing of plagioclase led to fluid infiltration, which initiated the dissolution of Ca-bearing plagioclase, which is out of equilibrium at greenschist facies (e.g. Stünitz, 1998), and the precipitation of equilibrium composition albite. During this reaction, the anorthite component of the original plagioclase contributed to clinozoisite formation and the albite component remained as now pure albite. This reaction is not quite balanced as clinozoisite has lower Ca/Al than anorthite, but it suffices to explain our general observations. Hydrated reaction products (e.g., clinozoisite) of the GSZ samples confirm that fluid was present while reactions were occurring.

When phases are out of equilibrium with a fluid they will dissolve, and a more stable phase will precipitate (i.e. nucleate and grow), but the processes of dissolution and precipitation can be coupled or uncoupled in space and time (Putnis, 2009). In the traditional model of dissolution and precipitation, the processes are uncoupled, e.g., during pressure solution, dissolution will occur at sites of high stress, and then be transported by diffusion to precipitate at sites of low stress. During interface-coupled dissolution-precipitation reactions, the processes occur simultaneously across a migrating reaction interface, preserving crystallographic orientation through the epitaxial nucleation of product phases. In the following two sections, we argue that both interface-coupled (section 5.2) and non-coupled (section 5.3) dissolution-precipitation operated in tandem to produce the different types of albite found in the GSZ metagabbros.

5.2 Interface-coupled dissolution and precipitation in large albite grains

Interface-coupled replacement occurs by a hydrated reaction front migrating through a crystal (Putnis, 2009). No reaction interfaces are preserved in the large albite grains of the low strain GSZ metagabbros, which have undergone complete albitisation. However, in this study we present strong microstructural and chemical evidence, gathered from naturally deformed, fully albitized rocks, that the large albite grains in the GSZ metagabbros have undergone interface-coupled replacement, and that this reaction has continued to completion during shearing. Key evidence and interpretations are discussed in detail in the remainder of section 5.2.

5.2.1 Lack of zoning

A complete lack of zoning in the large albite grains (Fig. 3) suggests that the "removal" of Ca from plagioclase was efficient and fast relative to lattice diffusion. Lattice diffusion of Ca can be discounted as an explanation for the lack of zoning due to the extremely low value of the interdiffusion coefficient, *D*, for CaAl-NaSi coupled substitution (required in the transition from Ca-bearing plagioclase to albite), at mid-crustal conditions. Experimentally derived values for the CaAl-NaSi interdiffusion coefficient over the temperature range 900–1100 °C, pressures of 1500 MPa, and 1 wt% H_2O are found to follow the Arrhenius relation $D = 3 \times 10^{-8} \exp(-303\ \text{kJ/mol})\ \text{m}^2\ \text{s}^{-1}$ (Liu and Yund, 1992). At 900 °C, this yields a D of ~$10^{-22}\ \text{m}^2\ \text{s}^{-1}$, and extrapolated to 500 °C (the upper limit of temperature indicated by the sample mineral assemblage; Prior and Wheeler, 1999), D slows to ~$10^{-30}\ \text{m}^2\ \text{s}^{-1}$. Lattice interdiffusion would therefore be extremely sluggish at greenschist facies conditions (Cherniak, 2010). The diffusion length formula $L = \sqrt{Dt}$ yields an estimate of $\sqrt{10^{-30} \times 3.154 * 10^{14}} = 1.78 * 10^{-8}$ m over a 10 Ma period. Thus, lattice interdiffusion would preserve zoning in grains of tens of μm to mm size over tens of Ma timescales (the timescale over which the Gressoney Shear Zone was active; Reddy et al., 1999). For these reasons, we discount Ca lattice diffusion as a viable mechanism for albitisation of the original, mm-scale Ca-bearing plagioclase grains, as a considerably faster mechanism must have been operating.

Experimental replacement of oligoclase and labradorite (i.e. Ca-bearing plagioclase) by pure Na end-member albite has been performed in an ^{18}O-enriched Na- and Si-bearing solution (Hövelmann et al., 2009). Oxygen isotope redistribution during these experiments has shown that the original Ca-bearing plagioclase framework breaks down entirely during replacement and new albite grains precipitate from the fluid, as opposed to the rearrangement of cations via some mechanism of enhanced ionic diffusion through an intact lattice. Replacement in the experiments is fast (reaction rims are 10s µm thick after 14 days), and as the entire crystal lattice is reconstituted with a new equilibrium composition, no zoning is observed in the product phase. Thus, interface coupled replacement is a viable mechanism by which the complete albitization of mm-cm-scale Ca-bearing plagioclase grains could have occurred in the low-strain metagabbros. A Ca-bearing phase, pectolite ($NaCa_2Si_3O_8OH$), is produced in the replacement experiments of Hövelmann et al. (2009), similar to the clinozoisite produced in the natural samples of this study.

5.2.2 Orientation inheritance

When metastable solids come into contact with fluids, dissolution can occur, causing the fluid to become supersaturated with respect to a more stable solid phase, which, depending on nucleation kinetics, may then precipitate. Nucleation is favoured (i.e. the energy budget is lower) when a product phase shares a similar crystallographic structure to the parent phase, so that new grains can nucleate on the surface of the dissolving parent grain (Putnis and John, 2010; Putnis and Putnis, 2007; Spruzeniece et al., 2017). This process is termed epitaxy (i.e. crystal growth on a crystalline substrate that determines orientation; Matthews, 1975), and leads to the product phase inheriting the orientation of the parent. Because the large albite grains in the low strain GSZ metagabbros do not contain preserved reaction fronts, it is difficult in most cases to know the original orientations of their parent grains, and thus whether orientations have been preserved during replacement. However, the grain presented in Figure 7, whose initial orientation is clear from its inclusion within a larger clinopyroxene grain, indicates that crystallographic orientation, including the detail of a twinning pattern, was preserved during complete replacement to albite. The preserved twin pattern is indicative of approximately pseudomorphic replacement, as described by Xia et al. (2009), which suggests that in this case, albite precipitation was the rate-limiting step. As other microstructural features, such as the characteristics of intracrystalline distortion (Spruzeniece et al., 2017), are shared between this grain and the other large albite grains (Figs. 4 and 6), we infer that the same replacement processes acted in all grains.

As a product phase precipitates during interface-coupled replacement, components of the solute are removed from the fluid, which increases the driving force for dissolution of the parent. Enhanced dissolution of the parent leads to enhanced precipitation of the product, until a steady state dissolution-precipitation rate is reached (Putnis and Putnis, 2007), and topotactic replacement (i.e. the conversion of an existing single crystal into a crystalline product which shares a crystallographic orientation with the original crystal; Shannon and Rossi, 1964) occurs. Under the right conditions (i.e. when the fluid pathways to the reaction front are kept open), such reactions can go to completion. As no reaction fronts are preserved in the large grains, this must have been the case for the GSZ metagabbros. We therefore propose that epitaxial nucleation followed by topotactic replacement can account for the complete albitization of large grains in the low strain metagabbros.

5.2.3 Lattice distortion in large albite grains

EBSD shows that the lattices of the large albite grains exhibit several degrees of internal distortion (Figs. 4, 6 and 7). The general consensus from nature (Kruse et al., 2001; Menegon et al., 2008; Menegon et al., 2013; Viegas et al., 2016; Wintsch and Yi, 2002) and experiment (Stünitz et al., 2003; Tullis, 2002; Tullis and Yund, 1992; Tullis and Yund, 1987) is that evidence for active slip systems in feldspar is rare at mid-crustal (T ~350–500 °C, P ~400–500 MPa) conditions. This is due to dislocations lacking mobility in feldspar at these conditions (Tullis and Yund, 1992). Therefore, intracrystalline distortion caused by crystal plasticity is not generally expected to be common in feldspar at greenschist facies.

The lattice distortion in the large albite grains is not interpreted to be inherited from deformation at higher grades as there is no evidence that the rocks of the GSZ ever experienced higher deformation conditions than greenschist facies (Prior and Wheeler, 1999; Wheeler and Butler, 1993). Even though the GSZ is interpreted to represent part of a reactivated subduction zone, Wheeler and Butler (1993) group the GSZ metagabbros as part of the Sesia Unit, which forms the overriding southern continental crust, on the basis that they are distinct from oceanic crustal gabbros observed in the Piemonte Unit.

As there was no basic magmatism in the Alpine orogeny, they are interpreted to be pre-Alpine basic intrusions into continental crust. Extension on the GSZ and associated shear zones exhumed eclogite facies rocks in the footwall (i.e. the Monte Rosa, Gran Paradiso and Dora Maira massifs), but the field evidence suggests the hanging wall never went to conditions above greenschist facies in the study region (Wheeler and Butler, 1993). In addition, there has been a metamorphic transition from Ca-bearing plagioclase to pure albite at greenschist facies, which would be expected to erase any pre-existing lattice distortion if the reaction had occurred by classical nucleation and growth, because this would form completely new crystals. A transition from oligoclase to albite by interface-coupled replacement in natural samples has previously been reported to result in distorted crystals identified by complex TEM diffraction patterns (Engvik et al., 2008), and the results of experiments performed on feldspar under static conditions also show intracrystalline distortion at the reaction interface (Hövelmann et al., 2009). In addition, Spruzeniece et al. (2017) showed that coupled replacement experiments on analogue materials (replacement of KBr by KCl) can produce deformation-resembling microstructures, including lattice distortion, in the absence of deformation. The lattice distortion observed in the GSZ metagabbros is therefore interpreted as a product of interface-coupled replacement of Ca-bearing plagioclase to albite. The WBV results presented in Figure 7 show that the <010> crystallographic direction is common in the Burgers vector population of the distorted large grains in the GSZ samples. This is not a direction that has previously been identified in plagioclase slip systems, e.g. (Stünitz et al., 2003), so is taken as further strong evidence that the observed dislocation network is not derived from crystal plasticity.

Instead, the distortion observed in the samples of this study can be explained as a result of imperfect replacement during fluid-assisted, interface-coupled reactions, due to a lattice mismatch between Ca-bearing plagioclase and pure albite. These type of growth defects are well-known in the materials science community, and are termed misfit dislocations e.g. (Matthews and Blakeslee, 1974). A lattice misfit during epitaxial/topotactic growth can be accommodated either by misfit dislocations, or by misfit elastic strain, or a combination of both (Jain et al., 1997; van der Merwe, 1991; Vdovin, 1999). Growth defects would effectively be ‘frozen in’ to the albite microstructure as slow diffusion rates restrict the climb (from one lattice plane to another) of dislocations in feldspar at the formation conditions of the middle crust (Tullis, 2002).

Some subgrain wall traces in the core of the large albite grain (Fig. 6), colour-coded blue (<010> Burgers vectors) and light green (<100> Burgers vectors) tend to be oriented WNW–ESE, subparallel to the trace of {110} crystal faces (poor cleavage), while red (<001> Burgers vectors) boundary traces tend to be oriented broadly NNE–SSW, subparallel to traces of {001} crystal faces (perfect cleavage). A crystal diagram of the orientation of crystal faces can be found in section S2 of the supplementary material. These observations suggest some crystallographic control on the formation of the subgrain walls described. Such features may represent microcracks formed on parent plagioclase cleavage planes that have healed during interface coupled replacement (note this is only possible if cracks either experienced relative movement akin to twist boundaries, or exhibited wedge-shaped opening). Further work is needed to explain the formation of these subgrain walls and the observed <010>, <100> and <001> Burgers vectors, which, in this context are clearly not associated with known deformation slip planes.

5.2.4 Microporosity

For interface-coupled reactions to proceed and go to completion, fluid pathways to the reaction interface must be kept open. Transient porosity is therefore a key control in the evolution of such fluid-assisted reactions. Porosity can be generated by two means. Firstly, if the replacement is pseudomorphic, i.e. the original shape and dimensions are preserved, but the new phase has a smaller molar volume, as a necessity, porosity will be generated during interface-coupled reactions (Putnis, 2009). Engvik et al. (2008) cite the 5% volume decrease between oligoclase and albite as a source of lattice distortion at the reaction interface. External dimensions and crystallographic orientations across replacement interfaces have been observed to be preserved in feldspar reactions (Engvik et al., 2008; Hövelmann et al., 2009; Putnis, 2002; Putnis and Putnis, 2007), so the volume decrease is likely to have resulted in the generation of transient porosity. An additional consideration is that the results of experiments that used ^{18}O to track how intact the plagioclase crystal lattice remains during interface-coupled reactions suggest that the entire lattice breaks down and is reconstructed during replacement

(Hövelmann et al., 2009). If more solid is dissolved than precipitated in this scenario, it will also result in development of porosity (Putnis and Putnis, 2007). Both these mechanisms could have contributed to the generation of transient porosity in the studied samples. In the cores of the large albite grains in the GSZ samples, intragranular microporosity, and intragranular product phase inclusions that record transient porosity, are observed (Fig. 2b–c; compare Fig. 2c to Fig. 3a of Putnis, 2015). These observations indicate further that the large distorted albite grains are the product of interface-coupled replacement.

Interface-coupled replacement can occur across tens of km^2 if the reactions proceed by either or both of these porosity-generating mechanisms (Plümper et al., 2017). If porosity generation ceases, or fluid access to the migrating reaction front is otherwise restricted, replacement reactions can terminate abruptly, preserving a sharp reaction interface (e.g. Engvik et al., 2008; Giuntoli et al., 2018). Such an interface is not preserved in the large albite grains, indicating the coupled replacement reactions went to completion.

In summary, despite the absence of a preserved reaction front due to reactions going to completion, the conclusion that large albite grains in the GSZ metagabbros formed by fluid-mediated, interface-coupled replacement reactions is supported by the following criteria:

1. A lack of zoning in a phase where it is otherwise common, indicating enhanced reaction kinetics (Putnis, 2009; Fig. 3).

2. Observation of intragranular microporosity or the signature of transient microporosity, and second phase inclusions which share orientations with twin and cleavage planes of porphyroclasts (Putnis and Putnis, 2007; Figs. 2 and 7).

3. The preservation of crystallographic orientation during replacement of parent grains (Hövelmann et al., 2009; Xia et al., 2009; Fig. 7).

4. Observation of a highly distorted lattice when crystal plastic lattice distortion is not expected at the conditions of deformation (Engvik et al., 2008; Hövelmann et al., 2009; Figs. 4 and 6).

5. Unexpected Burgers vectors that have not been identified in crystal plastic slip systems of the mineral under analysis (Fig. 6).

These criteria can be applied to any other replacement system. Their application could allow the products of replacement reactions to be identified even when complete replacement on a regional scale (e.g. Plümper et al., 2017) has taken place. This list complements the points highlighted by Spruzeniece et al. (2017), who showed that experimental products of interface-coupled replacement can contain deformation-resembling features, and suggested a list of microstructural indicators that can be used to distinguish replacement reaction-derived microstructures from deformation textures, including some criteria that depend on reaction fronts or parent grains being preserved. Our list is based on the detailed study of natural samples that have undergone complete replacement, and adds extra criteria that can be used to identify replacement reactions even when reactions have gone to completion, where reaction fronts have not been preserved. As Spruzeniece et al. (2017) stress, it is the cumulative presence of multiple criteria, rather than single features alone from this list, that can be used to diagnose interface-coupled dissolution-precipitation reactions.

5.3 Dissolution-precipitation reactions in fine-grained albite bands

The small grains do not exhibit the same microstructural features as the large grains. In particular, small grains lack the intragranular porosity and distortion which is characteristic of the large grains, therefore we infer they are not the product of interface-coupled replacement. The bands of small grains are oriented subparallel to the overall fracture geometries that can be observed at thin section scale (compare red box in Fig. 1c and e with Fig. 4). The microstructure in the bands of small grains, however, is not reminiscent of growth into dilatant sites (Bons et al., 2012). The shared orientation relationships between small grains and adjacent large grains may shed some light on their genesis.

Band B in Figure 4 has smaller grains with orientations that are closer to the large grain orientation compared to the grains in band A, whose grains are slightly larger and orientations more dispersed relative to the large grain (see also pole figures in Fig. 5). This orientation relationship could be achieved if the small grains are formed from nuclei of fragments of the original parent (Stünitz et al., 2003), where more fragments are produced in wider fractures that accommodate larger displacement, which results in greater rotations of the fragments. The fine-grained tail of the albite grain presented in Figure 7 strongly suggest that small grains are derived from fracturing of the adjacent large grains, and that orientation relationships can be preserved during this process, as the signature of twinning that was preserved in the large grain has also been preserved in the tail.

Giuntoli et al. (2018) present evidence for coupled replacement processes leading to the formation of small grains that have strong orientation relationships with larger grains (i.e. low angle boundaries, so they are technically classed as subgrains, but are not formed through crystal plastic processes). Those authors conclude that the small grains grew epitaxially as reaction products from slightly rotated fracture fragments via coupled dissolution-precipitation, which resulted in shared orientation. Although microstructures in the GSZ metagabbros suggest that the shared orientations of the large and small grains are related to fracturing, we do not see intragranular evidence (criteria 2, 4 and 5 in section 5.2.5) that the small grains formed by coupled replacement (i.e. they are free of internal microporosity and lattice distortion, and hence do not exhibit unexpected Burgers vectors).

We instead propose that small grain nuclei were derived from fragments of the parent grain, due to comminution along fracture surfaces, which underwent various degrees of rotation. In some cases, such as in band B, rotations were clearly small, but greater fragment rotation occurred in wider fractures (band A). This is consistent with the dispersion patterns observed in the pole figures in Figure 5, where dispersion occurs predominantly around the centre of the pole figures. This may record rigid body rotations of fragments around the bulk vorticity axis of the shear zone (e.g. Menegon et al., 2013). Due to the increased surface area of small fragments it is likely that they underwent almost complete dissolution and survived as nano-scale fragments that acted as precipitation nuclei. The lack of intracrystalline distortion in the small grains observed in this study suggests they grew on nano-fragments by precipitation in a supersaturated fluid. This phase of precipitation was *un*coupled from dissolution in time and space (see section 5.4.), so the porosity and distortion characteristic to coupled replacement did not develop.

Fragments generated by fracturing were proposed to act as nuclei for new grains during dynamic recrystallisation in feldspar by Stünitz et al. (2003). However, those observations were based on plagioclase that was deformed experimentally under dry conditions at 900 °C and 1 GPa, whereas the samples of this study were deformed at lower temperatures (~450 °C) under fluid-present conditions, which would encourage precipitation of new phases rather than dynamic recrystallisation. Stünitz et al. (2003) observed new grains with high-angle boundaries forming from fragments. In the metagabbros of this study, although the small albite grains in bands A and B exhibit a clear shared orientation with the large grains (Fig. 5), the misorientations between grains are in fact high-angle (i.e. > 15°), similar to the rotated fragments described by Stünitz et al. (2003), although the microphysical processes behind their formation are different. Band A is wider than band B (Fig. 4), and is interpreted to have accommodated greater displacement than band B. A comparison of the spread in pole figure maxima of the two bands suggests that if movement on fractures is small, fragment rotation will be limited, and stronger orientation relationships will be preserved (Fig. 5b and c).

Fragments generated by cataclasis typically have straight edges, angular shapes, and a large spread in grain size distribution (Stünitz and Fitz Gerald, 1993). In the Gressoney metagabbros, small grains in bands A and B (Figs. 4–5) and in the tail of the pseudomorphic grain (Fig. 7) do not exhibit these features, but instead show evidence for textural coarsening (120° triple junctions, curved boundary segments, relatively equant grain shapes), demonstrating that the microstructure has been substantially modified since initial fragmentation took place.

5.4 Microstructural evolution of feldspar in the gabbroic rocks of the GSZ at low strain

The GSZ is a km-wide shear zone responsible for the exhumation of eclogites in its footwall (Reddy et al., 2003; Wheeler and Butler, 1993). In this section, we address how deformation and dissolution-precipitation reactions combined in feldspar-rich lithologies to contribute to strain accommodation on the shear zone. The key stages of microstructural evolution are outlined in Figure 8.

FIGURE 8 HERE

For dissolution and precipitation to occur, fluid must be present. The microstructural evidence presented in section 5.1 indicates that brittle fracturing of the gabbros preceded fluid influx (Figs. 1 and 8a). Two types of dissolution-precipitation reactions are observed in the low-strain GSZ metagabbros. Where initial fracturing led to fluid infiltration into cracks, *un*coupled dissolution and precipitation occurred. Dissolution in this case almost completely consumed comminuted fragments of large Ca-bearing plagioclase grains on fracture surfaces, but it is likely that precipitation of albite began on fragment nuclei, hence preserving a signature of the parent grain orientation in the population of new fine-grained albite (Figs. 4, 5 and 8b). Precipitation of new strain-free albite healed initial fractures to form the bands of fine grains that cross-cut the distorted large grains (Figs. 2a, 4 and 8b). Under the conditions of Earth's middle crust, displacement along small grain-filled fractures is likely to have occurred by viscous flow (fluid-assisted diffusion creep, i.e. pressure solution) of the fine-grained bands (Fig. 8b). The precipitated new grains are a few orders of magnitude smaller than the original plagioclase. Note that the new grains are strain-free because the dissolution and precipitation was uncoupled – the dissolved components of albite were transported by diffusion to the sites where they precipitated, unlike in interface-coupled replacement, where precipitation of the new phase occurs at the dissolution interface (i.e. hydrous reaction front) and imperfect epitaxy can load the product phase with misfit dislocations (Matthews and Blakeslee, 1974).

On the basis of the interpretations listed in section 5.2, interface-coupled dissolution-precipitation is thought to account for the transformation of original Ca-bearing plagioclase to albite in parts of grains that did not undergo fracture. The interface-coupled replacement reactions in this model begin at fracture or boundary surfaces, or along cleavage or twin planes and migrate into the core of the grain (Fig. 8b), preserving the original crystallographic orientation of the parent (Fig. 7). Reactions along twin/cleavage planes form hydrous product phases that are oriented along those planes (Figs. 2b and 8c). The interface-coupled replacement reactions load product grains with a high dislocation density due to the production of misfit dislocations during imperfect epitaxy (Figs. 4b, 6 and 8d).

In the conceptual model presented in Figure 8, both coupled and non-coupled dissolution-precipitation occur in parallel, to produce large, distorted grains and small, undistorted grains of the same composition, in adjacent regions of grains. Why should two types of dissolution-precipitation occur in tandem in such close proximity? Putnis (2009) explains that for epitaxial replacement to occur, rates of dissolution and nucleation must be coupled at the reaction interface. This is achieved when the dissolution rate controls the reaction, and the activation energy for nucleation is relatively low, as is the case when the structure of an existing lattice is ‘borrowed’ to facilitate nucleation. In contrast, fast dissolution and sluggish nucleation can result in complete loss of coupling (Putnis, 2009). Because both processes listed above involve some degree of epitaxial nucleation, as recorded by orientation inheritance in both large and small albite grains, we speculate that fluid flux through fractures led to a decoupling of dissolution and precipitation, as dissolved components were transported away from the interface, so that the small new grains were produced by precipitation at new sites, even though nucleation was still facilitated by formation on existing plagioclase fragments. On the other hand, where hydrous reaction fronts migrated through unfractured parts of grains, transport of dissolved components was relatively inhibited, promoting interface-coupled replacement. A similar difference in dissolution-precipitation mechanisms related to fracture-controlled permeability and fluid flow is described by Moore et al. (2020). Those authors studied amphibolite-facies hydration of anorthositic granulites, showing that minerals growing within fractures exhibited textures characteristic of growth in a free fluid (curved-planar grain boundaries with common 120° triple junctions, indicating low interfacial energy), which are similar to the textures observed in the fine-grained bands of this study, particularly band A (Fig. 4). Amphibolite-facies minerals grown further away from the fractures (in the fracture damage zones, where fluid was still present but permeability was lower) showed microstructures characteristic of interface-coupled dissolution and precipitation (Moore et al., 2020), comparable to the large albite grains of this study. Differences in relative fluid flux in an open fracture environment and a migrating reaction front environment would also be likely to result in different requirements for fluid supersaturation to be achieved. Further, the dissolution rate of a group of comminuted fragments in fractures would have been faster than the same volume of unfractured plagioclase, due to the former’s substantially increased surface area available for reaction. These factors may have played a role in determining whether dissolution or nucleation was the rate controlling step in the respective regions of plagioclase, and therefore whether coupled or uncoupled dissolution-precipitation occurred. These interpretations are supported by the supposition of Xia et al. (2009) that the textures that form by interface-coupled dissolution-precipitation are dependent on whether dissolution, precipitation, or transport is the rate-limiting step.

5.5 Higher strain samples and future work

At higher strains, the GSZ metagabbros lack the large clasts observed at low strain (Jiang et al., 2000; Prior and Wheeler, 1999). The higher strain samples have a matrix composed predominantly of a mixture of fine-grained albite and clinozoisite (Prior and Wheeler, 1999), in which the grain size of albite is approximately the same size as the grains in the fine-grained bands shown in Figure 4. We propose that complete grain size reduction in higher strain samples took place by a combination of greater comminution of original plagioclase grains, and large clast fragments that underwent interface-coupled replacement were partly consumed by new strain-free grains, a process driven by strain energy due to the high dislocation density resulting from imperfect topotactic growth during interface-coupled replacement reactions. This hypothesis will be explored further in future work. Grain size reduction is understood to be critical to localising strain and the development of shear zones, and can lead to a switch to the grain-size sensitive deformation mechanisms diffusion creep or pressure solution (De Bresser et al., 2001; Fitz Gerald and Stünitz, 1993; Kilian et al., 2011; Rutter and Brodie, 1988; Tullis et al., 1990; Viegas et al., 2016). In the low strain samples presented here, evidence for such processes is limited, although the patterns in the pole figures in Figure 5 show increasing dispersion in larger fractures that accommodate greater offset. This is likely to record a component of rigid-body rotation, as discussed in section 5.3, but may also record rotations that are inherent to diffusion creep/pressure solution (e.g. Wheeler, 2009; 2010). The high strain samples presented in Prior and Wheeler (1999) and Jiang et al. (2000) are described as 'low-grade mylonites'. We therefore suggest that brittle fracturing and associated fluid influx led to two types of dissolution-precipitation reactions that acted in parallel in feldspar in the GSZ metagabbros, and consequently led to a grain size reduction of a few orders of magnitude which was responsible for the localization of strain and mylonitization of the original gabbros.

The breakdown of coarse-grained Ca-bearing plagioclase to a fine-grained mixture of albite and clinozoisite documented in this study has important geodynamic implications. At higher strains, the matrix of the GSZ metagabbros is predominantly composed of a well-mixed two-phase aggregate of albite and clinozoisite, which is likely to have inhibited grain growth by boundary pinning, encouraging grain-size sensitive deformation by diffusion creep/pressure solution (Brodie and Rutter, 1985; Herwegh et al., 2011; Kruse and Stünitz, 1999; Mehl and Hirth, 2008; Menegon et al., 2013; Pearce et al., 2011; Platt, 2015; Platt and Behr, 2011). Higher-strain data and the implications of such reaction softening in the GSZ metagabbros will be explored in future work. The microphysical processes outlined in this study detail a mechanism by which reaction softening is likely to occur over relatively short timescales compared to solid-state reactions, which underlines the importance of dissolution-precipitation reactions in the viscous behaviour of the crust.

6 Conclusions

Fracturing and associated fluid influx led to two types of dissolution-precipitation processes occurring in tandem, to convert Ca-bearing plagioclase feldspar to pure albite (An_0) in the GSZ metagabbros. Thin-section scale fracture patterns indicate fracturing was pervasive in all phases of the metagabbros. Where Ca-bearing plagioclase was fractured, comminution commonly occurred on fracture planes. Fracture healing by uncoupled dissolution of Ca-bearing fragments and precipitation of pure albite produced bands of fine-grained, strain free albite that cross-cut larger grains of the same composition. The large grains represent fragments of original Ca-bearing plagioclase that was transformed to pure albite through interface-coupled dissolution-precipitation.

Interface-coupled dissolution-precipitation was identified in the absence of preserved reaction by the presence of the following microstructural indicators: a lack of preserved zoning, indicating a fast reaction mechanism; orientation inheritance during reaction indicating epitaxial nucleation/topotactic replacement; lattice distortion at conditions where plastic deformation is not expected, plus the presence of Burgers vectors indicating distortion was not derived from crystal plasticity; intragranular microporosity and the presence of second phase inclusions which share orientations with twin and cleavage planes of their parent grains. These criteria could be applied to any system to identify interface-coupled replacement in the absence of preserved reaction fronts.

The combination of brittle fracturing and both types of dissolution-precipitation process led to an overall grain size reduction and a transition from brittle to viscous deformation. These processes worked to localize strain, producing mylonites and contributing to the development of a regional-scale shear zone.

Acknowledgments

This work was supported by the Natural Environment Research Council (Grant number NE/L002469/1). All EBSD and EDS datasets and SEM images were acquired in the EBSD-SEM laboratories, School of Environmental Sciences, University of Liverpool, now part of the University-wide SEM Shared Research Facility. We would like to thank Carmel Pinnington, Sarah Henton De Angelis and Matt Bilton for technical support during data collection.

References

Bestmann, M., Prior, D.J., 2003. Intragranular dynamic recrystallization in naturally deformed calcite marble: diffusion accommodated grain boundary sliding as a result of subgrain rotation recrystallization. Journal of Structural Geology 25, 1597-1613.

Bons, P.D., Elburg, M.A., Gomez-Rivas, E., 2012. A review of the formation of tectonic veins and their microstructures. Journal of Structural Geology 43, 33-62.

Brodie, K.H., Rutter, E.H., 1985. On the Relationship between Deformation and Metamorphism, with Special Reference to the Behavior of Basic Rocks, in: Thompson, A.B., Rubie, D.C. (Eds.), Metamorphic Reactions: Kinetics, Textures, and Deformation. Springer New York, New York, NY, pp. 138-179.

Bucher, K., Stober, I., 2010. Fluids in the upper continental crust. Geofluids 10, 241-253.

Cherniak, D.J., 2010. Cation Diffusion in Feldspars. Reviews in Mineralogy and Geochemistry 72, 691-733.

De Bresser, J., Ter Heege, J., Spiers, C., 2001. Grain size reduction by dynamic recrystallization: can it result in major rheological weakening? International Journal of Earth Sciences 90, 28-45.

Deer, W.A., Howie, R.A., Zussman, J., 2013. An introduction to the rock-forming minerals, 3rd ed. Mineralogical Society, UK.

Engvik, A.K., Ihlen, P.M., Austrheim, H., 2014. Characterisation of Na-metasomatism in the Sveconorwegian Bamble Sector of South Norway. Geoscience Frontiers 5, 659-672.

Engvik, A.K., Putnis, A., Fitz Gerald, J.D., Austrheim, H., 2008. Albitization of Granitic Rocks: The Mechanism of Replacement of Oligoclase by Albite. The Canadian Mineralogist 46, 1401-1415.

Fitz Gerald, J., Stünitz, H., 1993. Deformation of granitoids at low metamorphic grade. I: Reactions and grain size reduction. Tectonophysics 221, 269-297.

Giuntoli, F., Menegon, L., Warren, C.J., 2018. Replacement reactions and deformation by dissolution and precipitation processes in amphibolites. Journal of Metamorphic Geology 36, 1263-1286.

Glassley, W.E., 1998. Fluid–rock interaction, Geochemistry. Springer Netherlands, Dordrecht, pp. 248-250.

Gratier, J.-P., Dysthe, D.K., Renard, F., 2013. The role of pressure solution creep in the ductility of the Earth's upper crust. Advances in Geophysics 54, 47-179.

Gueydan, F., Leroy, Y.M., Jolivet, L., Agard, P., 2003. Analysis of continental midcrustal strain localization induced by microfracturing and reaction-softening. Journal of Geophysical Research: Solid Earth 108.

Herwegh, M., Linckens, J., Ebert, A., Berger, A., Brodhag, S.H., 2011. The role of second phases for controlling microstructural evolution in polymineralic rocks: A review. Journal of Structural Geology 33, 1728-1750.

Hildyard, R.C., Prior, D.J., Mariani, E., Faulkner, D.R., 2009. Crystallographic preferred orientation (CPO) of gypsum measured by electron backscatter diffraction (EBSD). Journal of microscopy 236, 159-164.

Hövelmann, J., Putnis, A., Geisler, T., Schmidt, B.C., Golla-Schindler, U., 2009. The replacement of plagioclase feldspars by albite: observations from hydrothermal experiments. Contributions to Mineralogy and Petrology 159, 43-59.

Humphreys, F.J., 2001. Review Grain and subgrain characterisation by electron backscatter diffraction. Journal of Materials Science 36, 3833-3854.

Jain, S.C., Harker, A.H., Cowley, R.A., 1997. Misfit strain and misfit dislocations in lattice mismatched epitaxial layers and other systems. Philosophical Magazine A 75, 1461-1515.

Jamtveit, B., Petley-Ragan, A., Incel, S., Dunkel, K.G., Aupart, C., Austrheim, H., Corfu, F., Menegon, L., Renard, F., 2019. The Effects of Earthquakes and Fluids on the Metamorphism of the Lower Continental Crust. Journal of Geophysical Research: Solid Earth 124, 7725-7755.

Jiang, Z., Prior, D.J., Wheeler, J., 2000. Albite crystallographic preferred orientation and grain misorientation distribution in a low-grade mylonite: implications for granular flow. Journal of Structural Geology 22, 1663-1674.

Kilian, R., Heilbronner, R., Stünitz, H., 2011. Quartz grain size reduction in a granitoid rock and the transition from dislocation to diffusion creep. Journal of Structural Geology 33, 1265-1284.
Kruse, R., Stünitz, H., 1999. Deformation mechanisms and phase distribution in mafic high-temperature mylonites from the Jotun Nappe, southern Norway. Tectonophysics 303, 223-249.
Kruse, R., Stünitz, H., Kunze, K., 2001. Dynamic recrystallization processes in plagioclase porphyroclasts. Journal of Structural Geology 23, 1781-1802.
Liu, M., Yund, R.A., 1992. NaSi-CaAl interdiffusion in plagioclase. American Mineralogist 77, 275-283.
Logan, J.M., Dengo, C.A., Higgs, N.G., Wang, Z.Z., 1992. Chapter 2 Fabrics of Experimental Fault Zones: Their Development and Relationship to Mechanical Behavior, in: Evans, B., Wong, T.-f. (Eds.), International Geophysics. Academic Press, pp. 33-67.
Marchesini, B., Garofalo, P.S., Menegon, L., Mattila, J., Viola, G., 2019. Fluid-mediated, brittle–ductile deformation at seismogenic depth – Part 1: Fluid record and deformation history of fault veins in a nuclear waste repository (Olkiluoto Island, Finland). Solid Earth 10, 809-838.
Matthews, J., 1975. Epitaxial growth. Academic Press, New York.
Matthews, J.W., Blakeslee, A.E., 1974. Defects in epitaxial multilayers: I. Misfit dislocations. Journal of Crystal Growth 27, 118-125.
Mehl, L., Hirth, G., 2008. Plagioclase preferred orientation in layered mylonites: Evaluation of flow laws for the lower crust. Journal of Geophysical Research 113.
Menegon, L., Pennacchioni, G., Malaspina, N., Harris, K., Wood, E., 2017. Earthquakes as Precursors of Ductile Shear Zones in the Dry and Strong Lower Crust. Geochemistry, Geophysics, Geosystems 18, 4356-4374.
Menegon, L., Pennacchioni, G., Spiess, R., 2008. Dissolution-precipitation creep of K-feldspar in mid-crustal granite mylonites. Journal of Structural Geology 30, 565-579.
Menegon, L., Stünitz, H., Nasipuri, P., Heilbronner, R., Svahnberg, H., 2013. Transition from fracturing to viscous flow in granulite facies perthitic feldspar (Lofoten, Norway). Journal of Structural Geology 48, 95-112.
Moore, J., Beinlich, A., Piazolo, S., Austrheim, H., Putnis, A., 2020. Metamorphic Differentiation via Enhanced Dissolution along High Permeability Zones. Journal of Petrology 61.
Mukai, H., Austrheim, H., Putnis, C.V., Putnis, A., 2014. Textural Evolution of Plagioclase Feldspar across a Shear Zone: Implications for Deformation Mechanism and Rock Strength. Journal of Petrology 55, 1457-1477.
Nye, J., 1953. Some geometrical relations in dislocated crystals. Acta metallurgica 1, 153-162.
Oliot, E., Goncalves, P., Marquer, D., 2010. Role of plagioclase and reaction softening in a metagranite shear zone at mid-crustal conditions (Gotthard Massif, Swiss Central Alps). Journal of Metamorphic Geology 28, 849-871.
Pearce, M.A., Wheeler, J., 2011. Grain growth and the lifetime of diffusion creep deformation. Geological Society, London, Special Publications 360, 257-272.
Platt, J.P., 2015. Rheology of two-phase systems: A microphysical and observational approach. Journal of Structural Geology 77, 213-227.
Platt, J.P., Behr, W.M., 2011. Grainsize evolution in ductile shear zones: Implications for strain localization and the strength of the lithosphere. Journal of Structural Geology 33, 537-550.
Plümper, O., Botan, A., Los, C., Liu, Y., Malthe-Sørenssen, A., Jamtveit, B., 2017. Fluid-driven metamorphism of the continental crust governed by nanoscale fluid flow. Nature Geoscience 10, 685.
Plümper, O., Putnis, A., 2009. The Complex Hydrothermal History of Granitic Rocks: Multiple Feldspar Replacement Reactions under Subsolidus Conditions. Journal of Petrology 50, 967-987.
Prior, D.J., Mariani, E., Wheeler, J., 2009. EBSD in the earth sciences: applications, common practice, and challenges, Electron backscatter diffraction in materials science. Springer, pp. 345-360.
Prior, D.J., Wheeler, J., 1999. Feldspar fabrics in a greenschist facies albite-rich mylonite from electron backscatter diffraction. Tectonophysics 303, 29-49.

Prior, D.J., Wheeler, J., Peruzzo, L., Spiess, R., Storey, C., 2002. Some garnet microstructures: an illustration of the potential of orientation maps and misorientation analysis in microstructural studies. Journal of Structural Geology 24, 999-1011.
Putnis, A., 2002. Mineral replacement reactions: from macroscopic observations to microscopic mechanisms. Mineralogical Magazine 66, 689-708.
Putnis, A., 2009. Mineral Replacement Reactions. Reviews in Mineralogy and Geochemistry 70, 87-124.
Putnis, A., 2015. Transient Porosity Resulting from Fluid–Mineral Interaction and its Consequences. Reviews in Mineralogy and Geochemistry 80, 1-23.
Putnis, A., John, T., 2010. Replacement Processes in the Earth's Crust. Elements 6, 159-164.
Putnis, A., Putnis, C.V., 2007. The mechanism of reequilibration of solids in the presence of a fluid phase. Journal of Solid State Chemistry 180, 1783-1786.
Randle, V., 2009. Electron backscatter diffraction: Strategies for reliable data acquisition and processing. Materials Characterization 60, 913-922.
Reddy, S., Wheeler, J., Cliff, R., 1999. The geometry and timing of orogenic extension: an example from the Western Italian Alps. Journal of Metamorphic Geology 17, 573-590.
Reddy, S.M., Wheeler, J., Butler, R.W.H., Cliff, R.A., Freeman, S., Inger, S., Pickles, C., Kelley, S.P., 2003. Kinematic reworking and exhumation within the convergent Alpine Orogen. Tectonophysics 365, 77-102.
Rutter, E.H., Brodie, K.H., 1988. The role of tectonic grain size reduction in the rheological stratification of the lithosphere. Geologische Rundschau 77, 295-307.
Rutter, E.H., Maddock, R.H., Hall, S.H., White, S.H., 1986. Comparative microstructures of natural and experimentally produced clay-bearing fault gouges. pure and applied geophysics 124, 3-30.
Shannon, R.D., Rossi, R.C., 1964. Definition of Topotaxy. Nature 202, 1000-1001.
Simpson, C., 1985. Deformation of granitic rocks across the brittle-ductile transition. Journal of Structural Geology 7, 503-511.
Spruzeniece, L., Piazolo, S., Maynard-Casely, H.E., 2017. Deformation-resembling microstructure created by fluid-mediated dissolution-precipitation reactions. Nat Commun 8, 14032.
Stünitz, H., 1993. Transition from fracturing to viscous flow in a naturally deformed metagabbro. Defects and processes in the solid state: geoscience applications: the Mc-Laren volume (Developments in Petrology, Vol. 4). Amsterdam, Elsevier Science, 121-150.
Stünitz, H., 1998. Syndeformational recrystallization–dynamic or compositionally induced? Contributions to Mineralogy and Petrology 131, 219-236.
Stünitz, H., Fitz Gerald, J., 1993. Deformation of granitoids at low metamorphic grade. II: Granular flow in albite-rich mylonites. Tectonophysics 221, 299-324.
Stünitz, H., Fitz Gerald, J.D., Tullis, J., 2003. Dislocation generation, slip systems, and dynamic recrystallization in experimentally deformed plagioclase single crystals. Tectonophysics 372, 215-233.
Stünitz, H., Tullis, J., 2001. Weakening and strain localization produced by syn-deformational reaction of plagioclase. International Journal of Earth Sciences 90, 136-148.
Tullis, J., 2002. Deformation of Granitic Rocks: Experimental Studies and Natural Examples. Reviews in Mineralogy and Geochemistry 51, 51-95.
Tullis, J., Dell'Angelo, L., Yund, R.A., 1990. Ductile shear zones from brittle precursors in feldspathic rocks: The role of dynamic recrystallization. 56, 67-81.
Tullis, J., Yund, R., 1992. Chapter 4 The Brittle-Ductile Transition in Feldspar Aggregates: An Experimental Study, in: Evans, B., Wong, T.-f. (Eds.), International Geophysics. Academic Press, pp. 89-117.
Tullis, J., Yund, R.A., 1987. Transition from cataclastic flow to dislocation creep of feldspar: Mechanisms and microstructures. Geology 15, 606-609.
van der Merwe, J.H., 1991. Misfit dislocation generation in epitaxial layers. Critical Reviews in Solid State and Materials Sciences 17, 187-209.

Vdovin, V., 1999. Misfit dislocations in epitaxial heterostructures: Mechanisms of generation and multiplication. PHYSICA STATUS SOLIDI A APPLIED RESEARCH 171, 239-250.
Vho, A., Rubatto, D., Lanari, P., Regis, D., 2020. The evolution of the Sesia Zone (Western Alps) from Carboniferous to Cretaceous: insights from zircon and allanite geochronology. Swiss Journal of Geosciences 113, 24.
Viegas, G., Menegon, L., Archanjo, C., 2016. Brittle grain-size reduction of feldspar, phase mixing and strain localization in granitoids at mid-crustal conditions (Pernambuco shear zone, NE Brazil). Solid Earth 7, 375-396.
Wheeler, J., 2010. Anisotropic rheology during grain boundary diffusion creep and its relation to grain rotation, grain boundary sliding and superplasticity. Philosophical Magazine 90, 2841-2864.
Wheeler, J., Butler, R.W., 1993. Evidence for extension in the western Alpine orogen: the contact between the oceanic Piemonte and overlying continental Sesia units. Earth and Planetary Science Letters 117, 457-474.
Wheeler, J., Mariani, E., Piazolo, S., Prior, D., Trimby, P., Drury, M., 2009. The weighted Burgers vector: a new quantity for constraining dislocation densities and types using electron backscatter diffraction on 2D sections through crystalline materials. Journal of microscopy 233, 482-494.
Wilkinson, A.J., Britton, T.B., 2012. Strains, planes, and EBSD in materials science. Materials Today 15, 366-376.
Wintsch, R., Yi, K., 2002. Dissolution and replacement creep: a significant deformation mechanism in mid-crustal rocks. Journal of Structural Geology 24, 1179-1193.
Xia, F., Brugger, J., Chen, G., Ngothai, Y., O’Neill, B., Putnis, A., Pring, A., 2009. Mechanism and kinetics of pseudomorphic mineral replacement reactions: A case study of the replacement of pentlandite by violarite. Geochimica et Cosmochimica Acta 73, 1945-1969.
Yardley, B.W.D., Bodnar, R.J., 2014. Fluids in the Continental Crust. Geochemical Perspectives 3, 1-127.

Figures

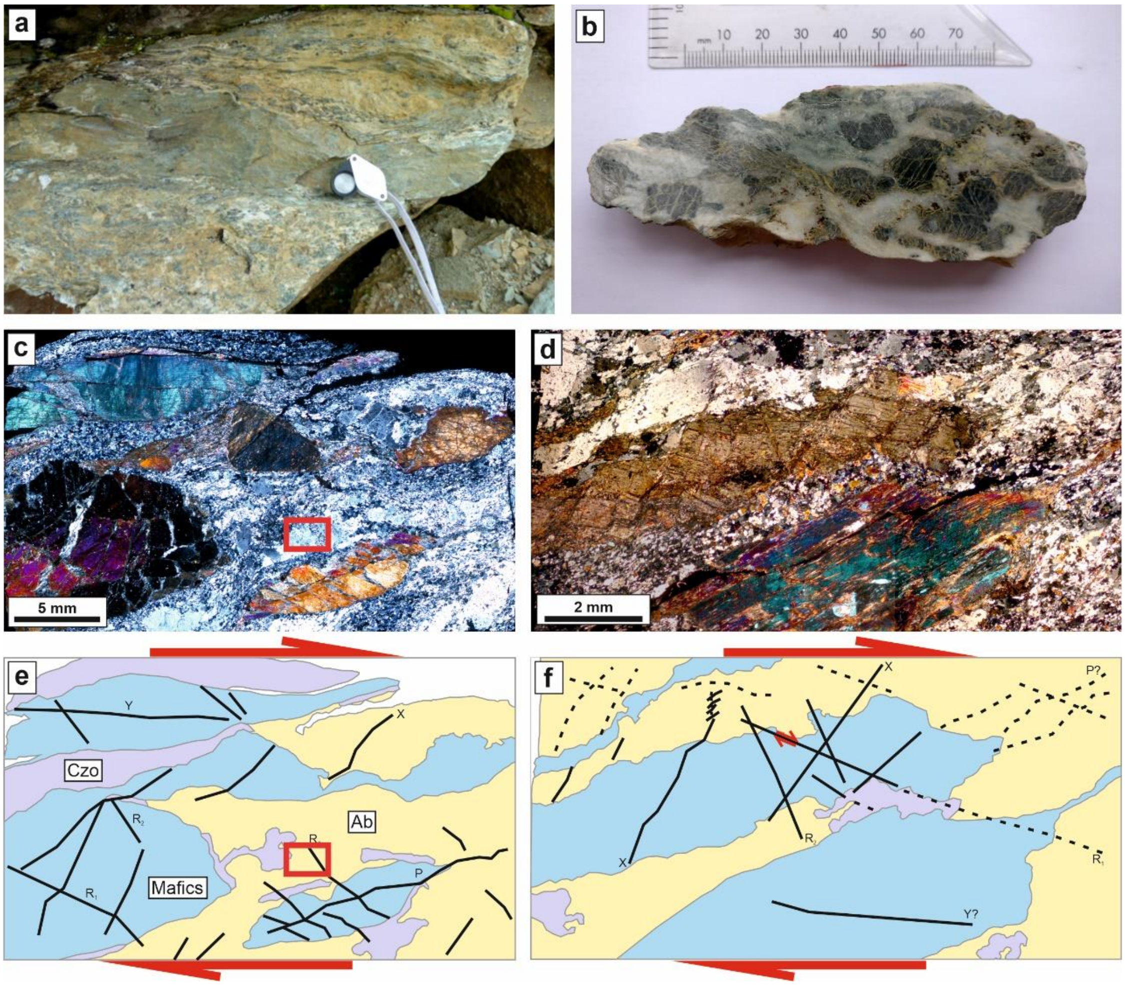

Figure 1 *a) Road cut exposure of low strain metagabbro. b) Slab of low strain metagabbro. c) XPL images showing fracture-related features on the thin-section scale. Large clinopyroxene porphyroclasts and albitic feldspar grains dominate the samples. Hornblende is present locally, often lining clinopyroxene. Actinolite occurs as reaction rims and in between fractured clinopyroxene. Albite occurs in a bimodal distribution: mm- to cm-scale grains are surrounded by smaller, μm-scale matrix grains, of the same composition (An_0). Red box indicates region shown in Figure 4. d) Detail of large clinopyroxene and albite grains showing through-going fractures cross phase boundaries, suggesting all phases in the original coarse-grained gabbro underwent brittle fracture. e) and f) are overlays of c) and d), respectively, showing that the observed fractures follow typical geometries of fracture sets, after Rutter et al. (1986). Thin sections were cut so that their long edges are parallel to the shear plane according to field observations and oriented hand specimens, but this may be subject to slight error due to the low strain of the rocks.*

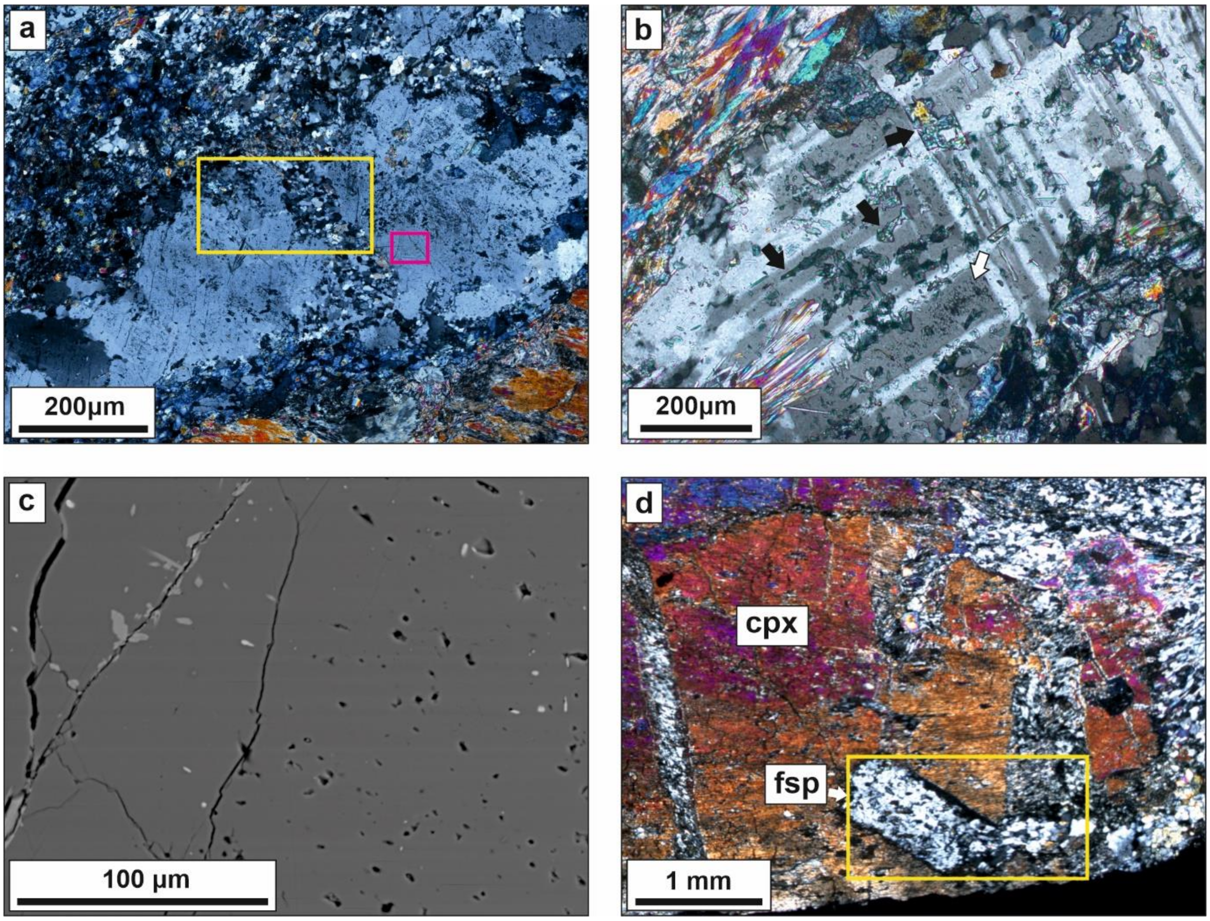

Figure 2 *a) XPL image of a large albite grain detailed in later figures (yellow box is region shown in Fig. 4; fuchsia box is region shown in Fig. 6). b) XPL image showing sets of intersecting twins within a large albite grain, showing secondary phase inclusions (mostly clinozoisite, some actinolite) aligned parallel to, and elongate in, the direction of twin plane traces (black arrows). Secondary phase inclusions are scattered throughout individual twin segments (white arrow); c) BSE image of distributed intragranular microporosity in the core of a large albite grain; d) XPL image showing a feldspathic inclusion within a fractured clinopyroxene grain which is mostly protected from deformation. Where a large fracture in the clinopyroxene cross-cuts the feldspar grain, it has undergone a grain size reduction and a tail of fine-grained albite has formed. Yellow box is region presented in Fig. 7.*

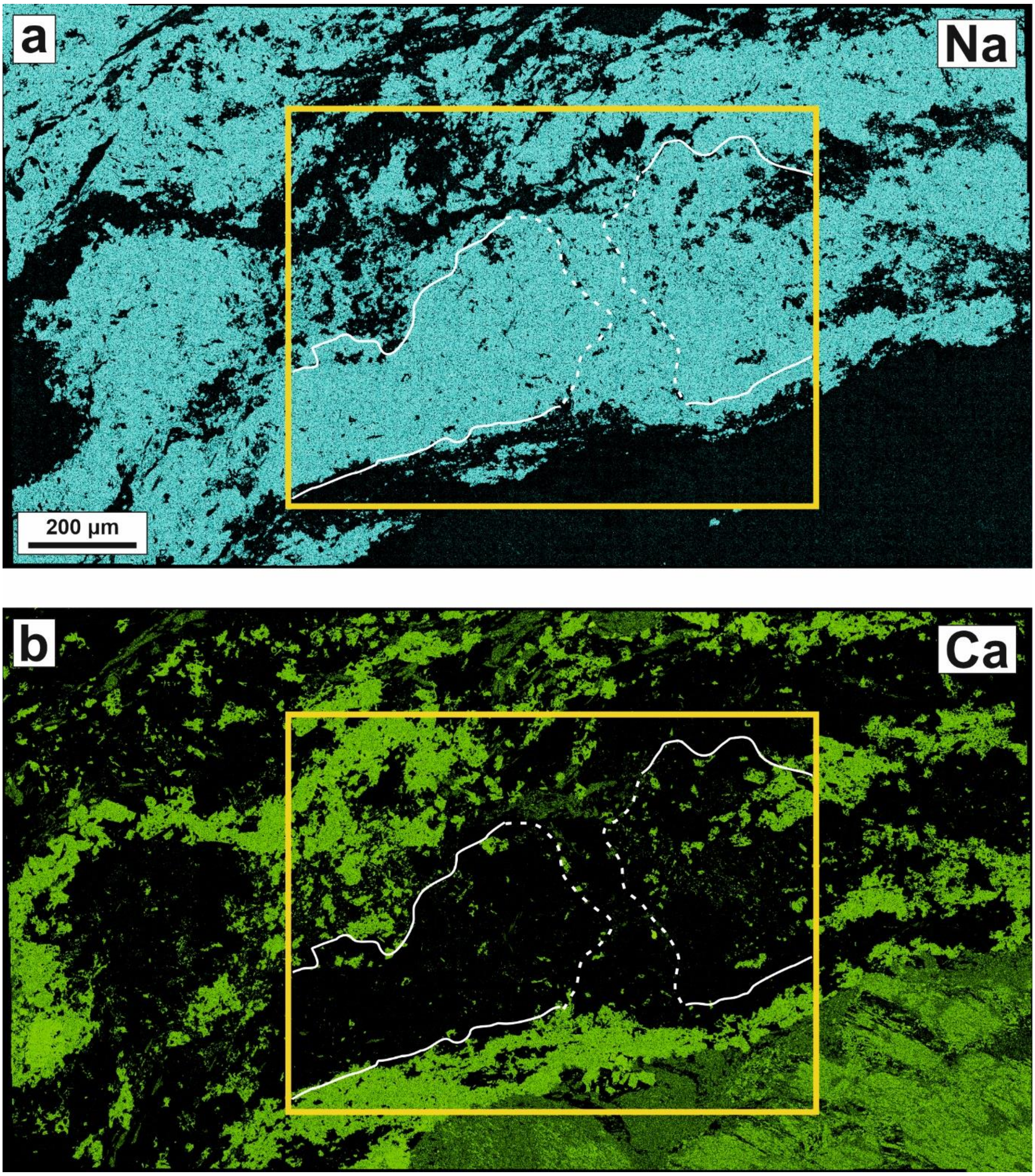

Figure 3 *Chemical maps of a) Na and b) Ca distribution in the large albite grain in Fig. 2a and surrounding matrix. Yellow box indicates region presented in Fig. 2a. White solid lines show approximate edge of large grain. White dashed lines show approximate edges of band of small grains labelled Band A in Fig. 4. Note complete lack of chemical zonation in the mm-scale grain. There is no difference in composition between the large grain and the small grains in the cross-cutting band (both An0).*

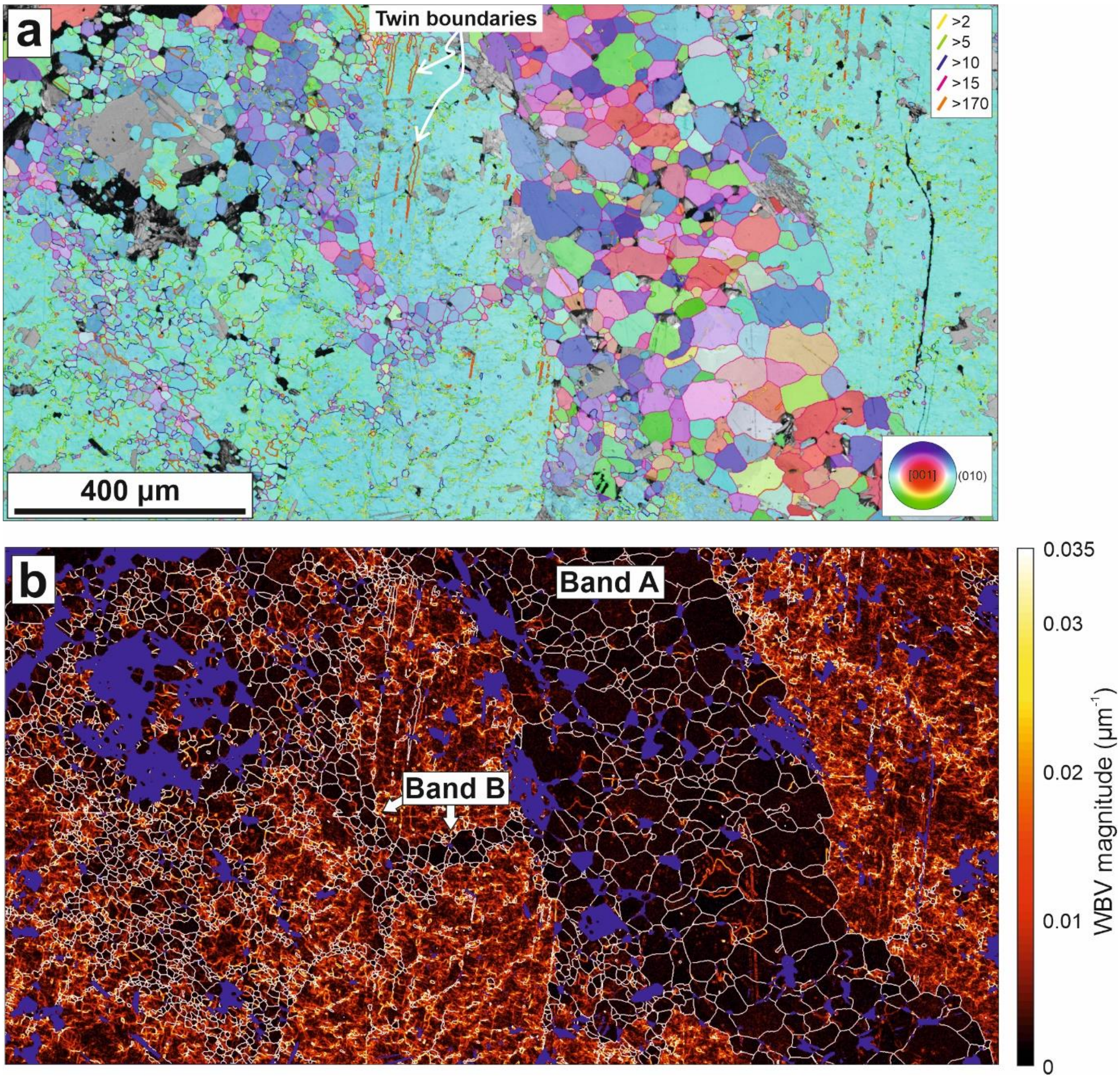

Figure 4 *a) EBSD map (Euler colour scheme) of the region defined by the yellow box in Fig. 2a. Different colours represent different crystallographic orientations. (Sub)grain boundaries are coloured with respect to boundary misorientations, in degrees, including the albite twin boundary (white). The core of the light blue albite grain is littered with subgrain boundaries displaying misorientations of 5° or less (yellow lines) that sometimes form discrete subgrains, but also occur as distributed networks. Bands of small grains run through the large grain, labelled A and B in part (b). Many of the small grains in bands A and B share orientations with the large grain (see also Fig. 5). The traces of the bands are orientated parallel to thin section-wide fracture traces P and* R_2 *(compare Fig. 1c–d). Nearly all small grains in the bands exhibit high-angle grain boundaries (> 15°, fuchsia), but some low-angle boundaries, and some pericline twin boundaries (>160°, orange) are also*

present. b) WBV magnitude map quantitatively represents the amount of intracrystalline distortion within large and small grains. As WBV magnitude is a proxy for dislocation density, the map shows that the large grains are highly distorted relative to the small grains in bands A and B, which are nominally free of intracrystalline strain. Other phases and non-indexed regions of the map are coloured dark blue.

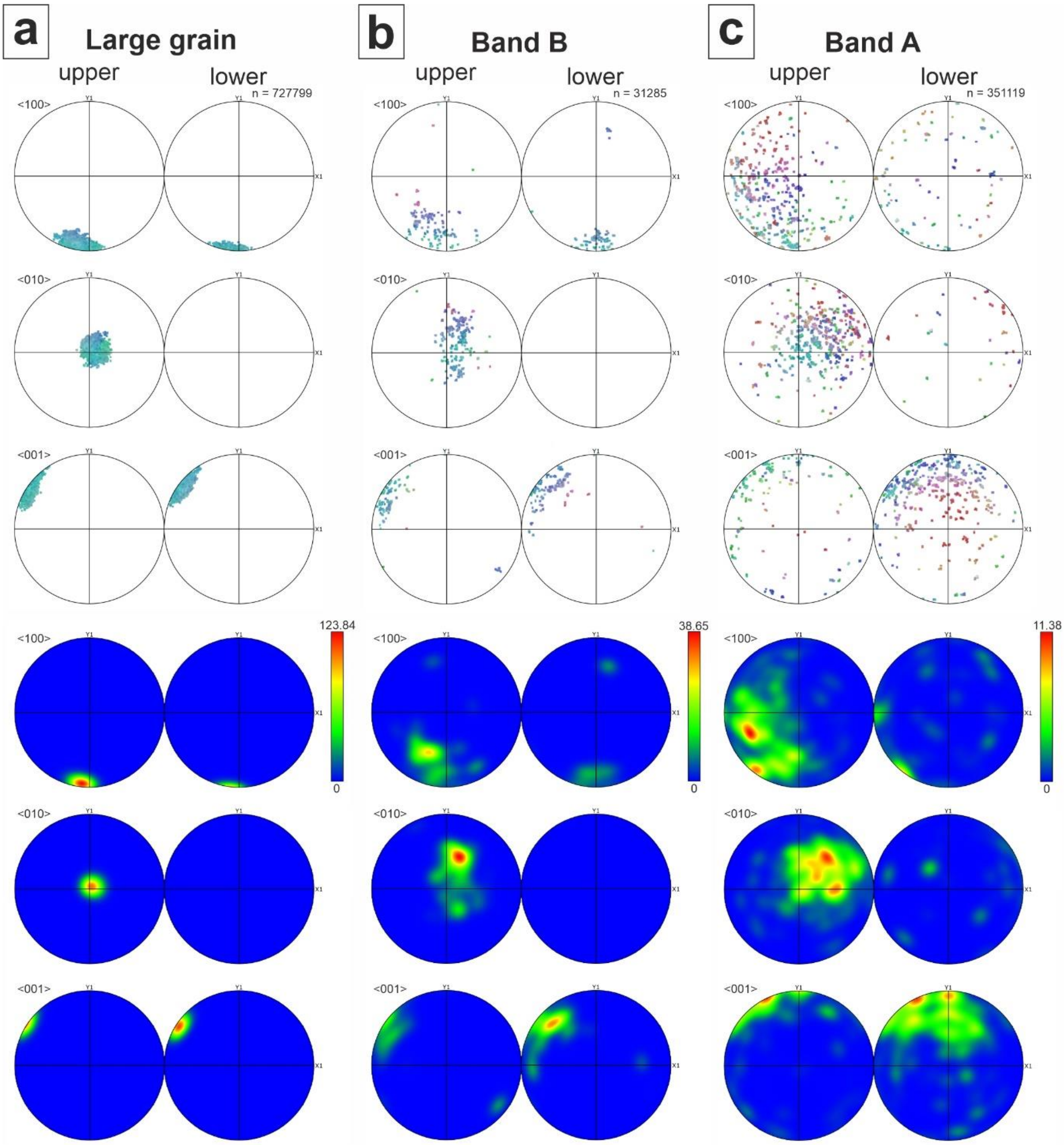

Figure 5 *Pole figures (top row all points, bottom row contoured) showing the orientation relationships between (a) the large albite grain, (b) the small grains in band B, and (c) the small grains in band A. Upper and lower hemispheres of the principal crystallographic directions are plotted. The large grain is oriented so that the [010] direction is perpendicular to the map plane. The orientation of the large grain is broadly shared by the small grains in both bands, with dispersion away from the single crystal distribution of the large grain increasing from the finer band B to the wider band A. Colour scales in the contoured plots have different maximum values, as strength of the maxima in (a) >> (b) >> (c). Contoured plots have a half width of 15°.*

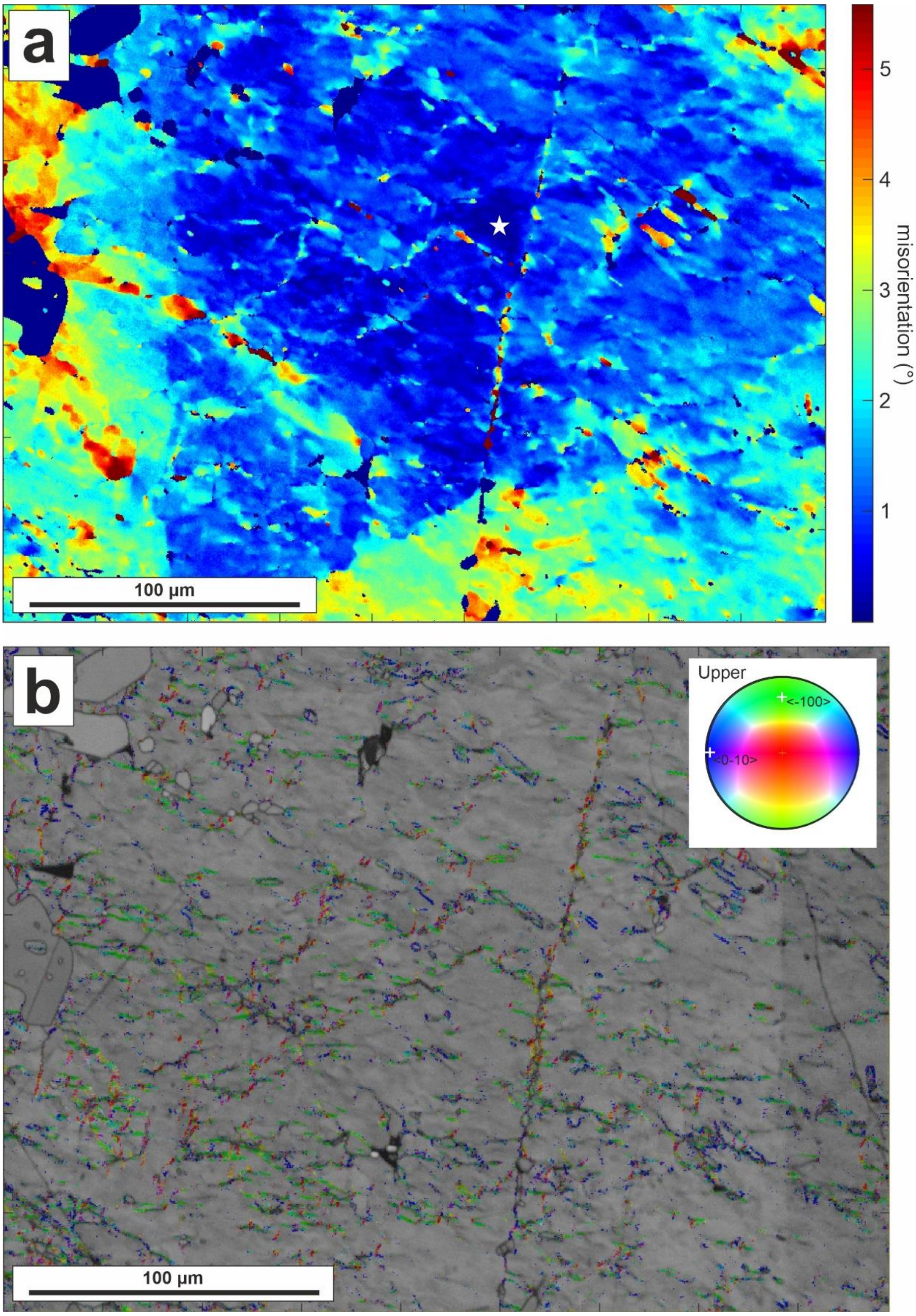

Figure 6 *a) EBSD map from a large albite grain core (fuchsia box in Fig. 2), showing intragranular misorientation calculated relative to white star. Ubiquitous low-angle distortion is present throughout the core of the grain; b) Band contrast EBSD map, with overlay showing directions of most likely Burgers vectors in dislocation structures (IPF colour scheme, key inset). Pixels with smallest calculated*

WBV magnitudes have been removed as they are prone to the highest angular errors. Blue, green and red pixels are common in the map. Blue in the colour scheme represents the <010> crystallographic direction, which is not a recognised slip direction in plagioclase feldspar.

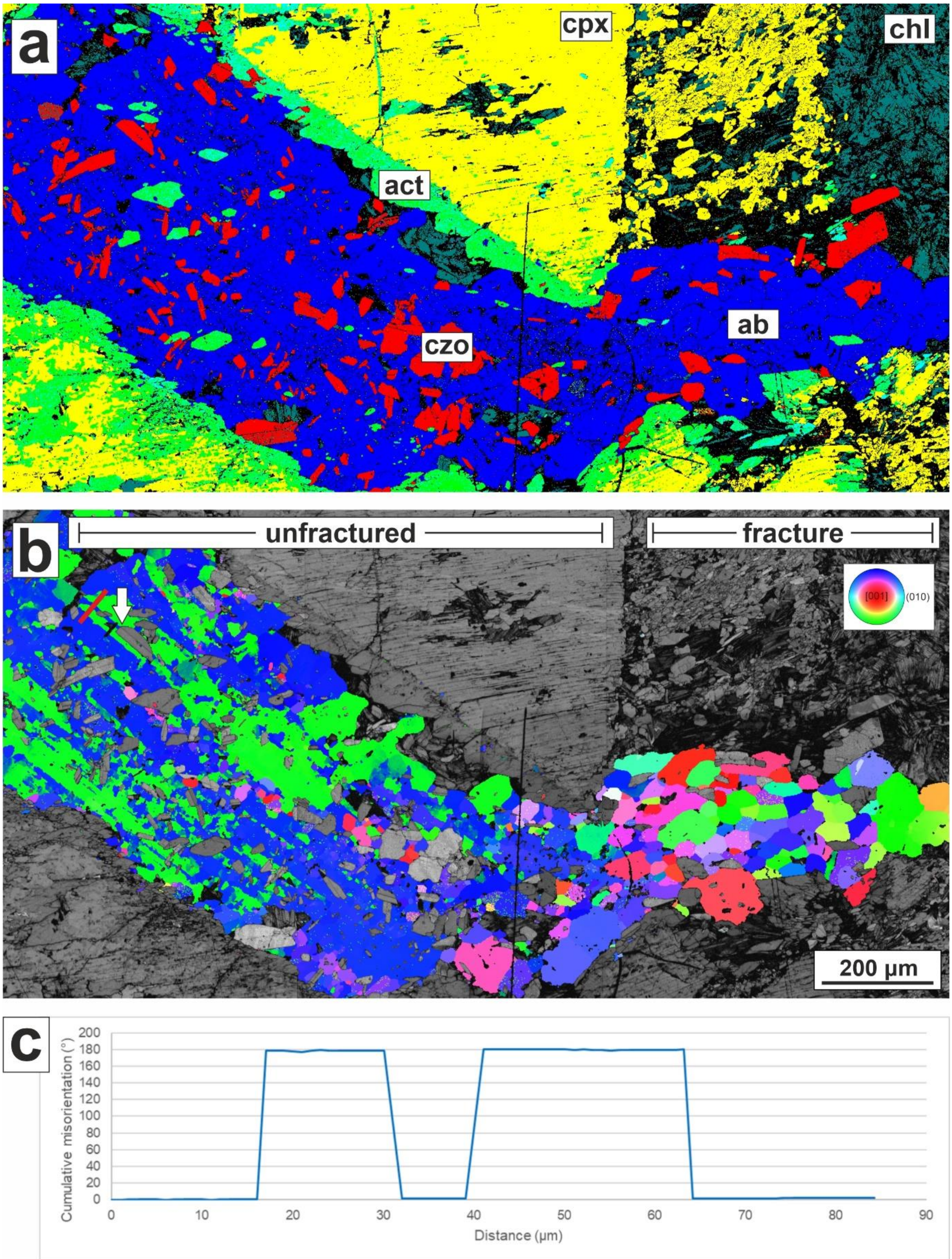

Figure 7 *EBSD maps showing an albite grain that formed by metamorphic replacement of original Ca-bearing plagioclase. a) Phase map showing distribution of greenschist facies reaction products. The albite grain contains abundant clinozoisite and actinolite inclusions. b) IPF-X map showing original*

twin orientations in the protected grain have been largely preserved during the transition from Ca-bearing plagioclase to albite (blue and green bands that run parallel to the long axis of the protected grain). A signature of twin orientations is also apparent in the tail of small grains, which are predominantly coloured blue and green, indicating an orientation relationship between the small tail grains and the large grain. Twin boundaries in the undeformed part of the large albite grain are no longer straight. An original plagioclase twin interface has been inherited by a twinned clinozoisite grain (white arrow). c) Misorientation profile showing 180° misorientation across twin planes, constructed from red line drawn in (b). See section S4 of the supplementary material for supporting pole figures.

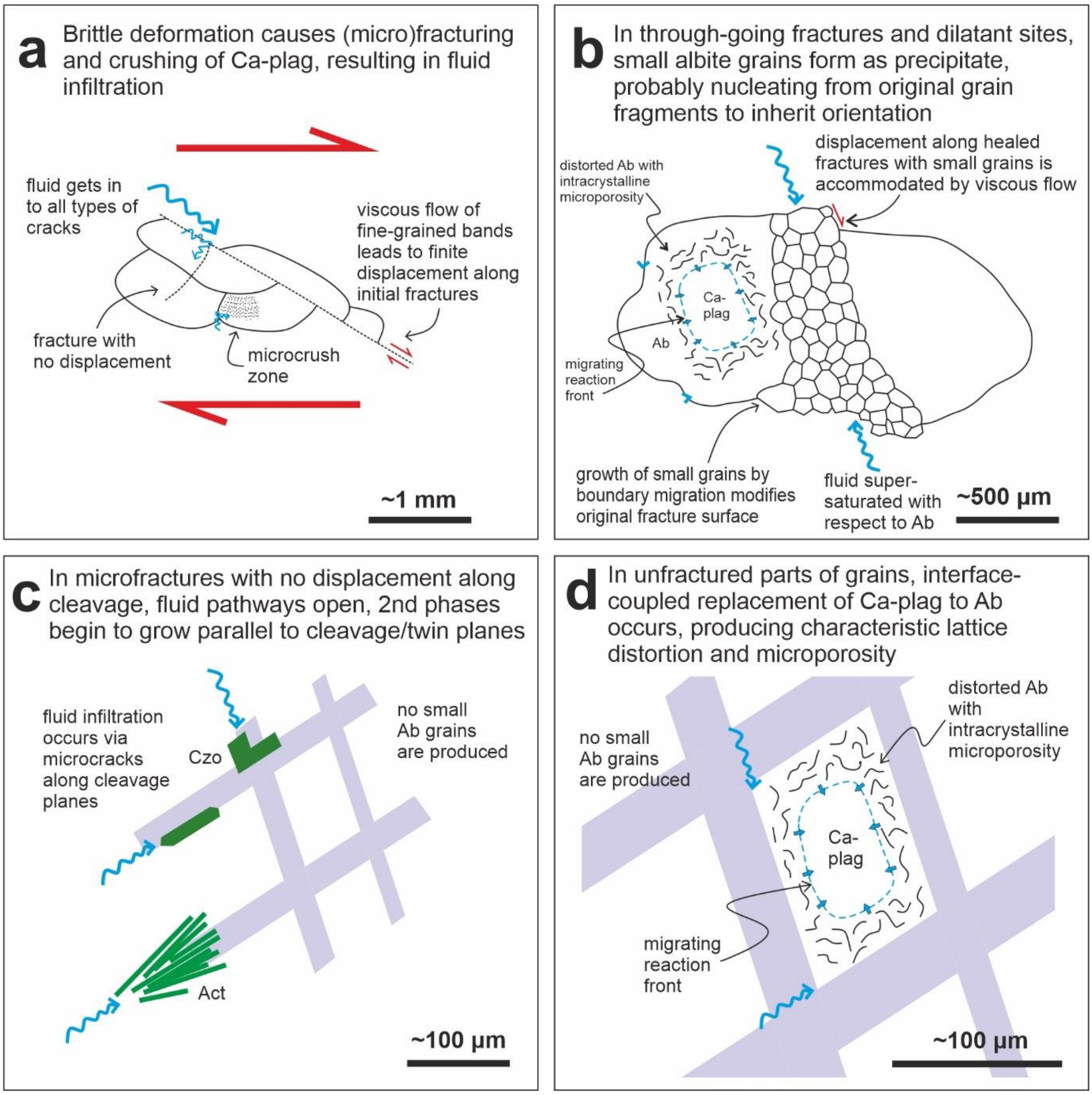

1042 ***Figure 8*** *Conceptual model. The dominant process in each part of the model is described in each of the boxes (a)–(d). Ab = albite, Czo = clinozoisite, Act = actinolite.*

Supplementary information

S1. Extra information about how pole figures in Figure 5 were created from subsets of Figure 4. All data was processed using Oxford Instruments' AZtecCrystal software.

Subset used to construct 'large grain' pole figures:

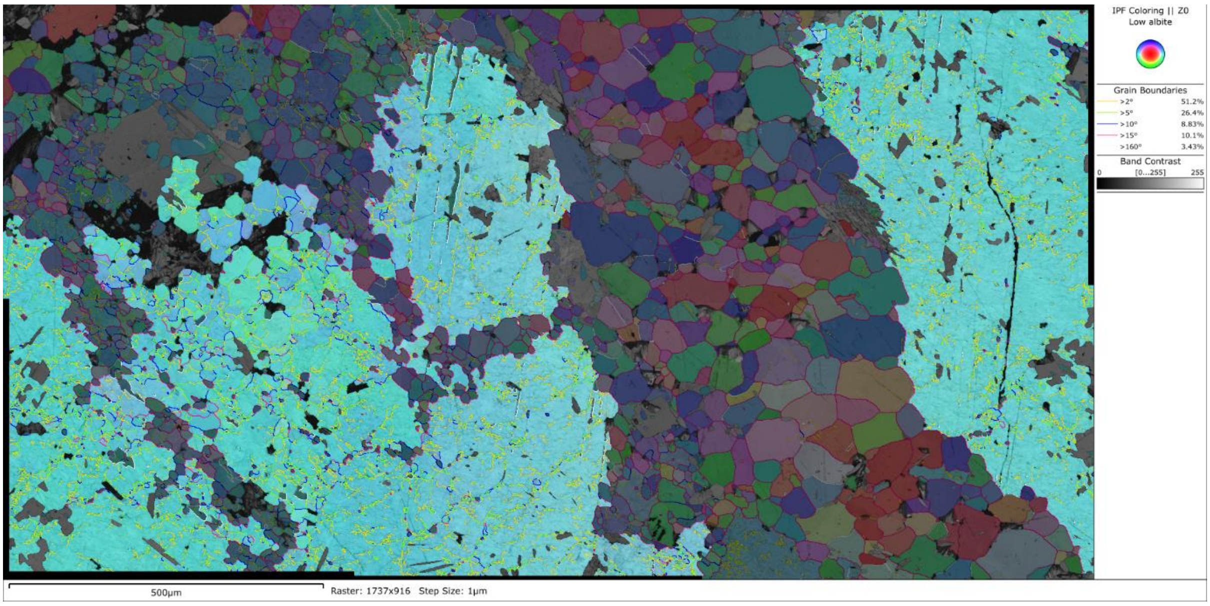

Subset used to construct 'Band A' pole figures:

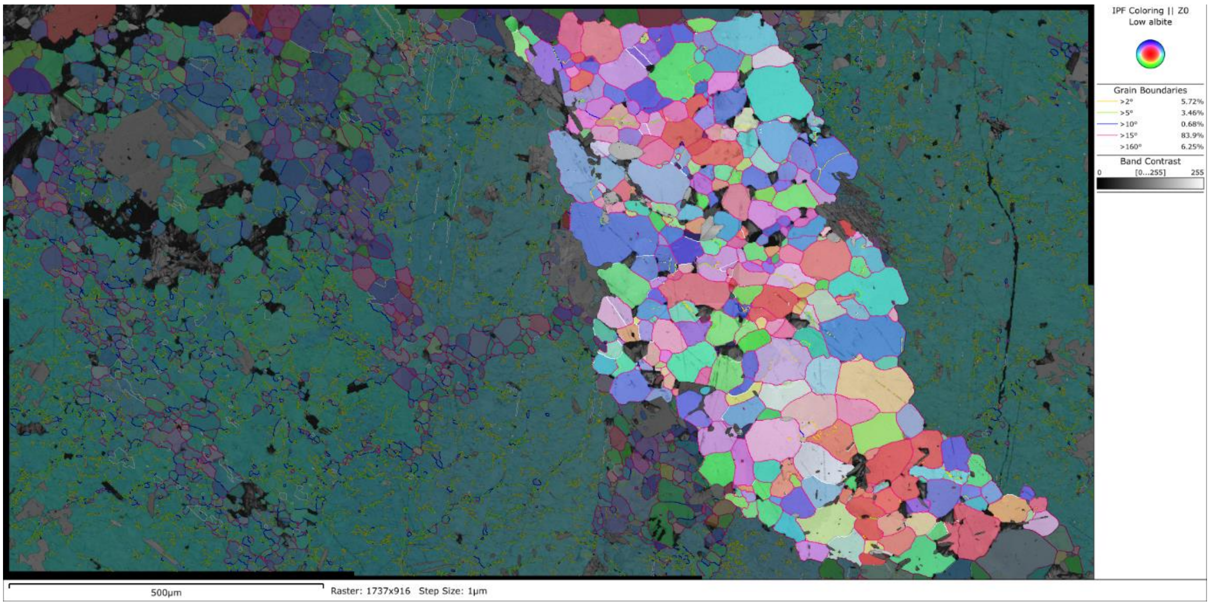

Subset used to construct ‘Band B’ pole figures:

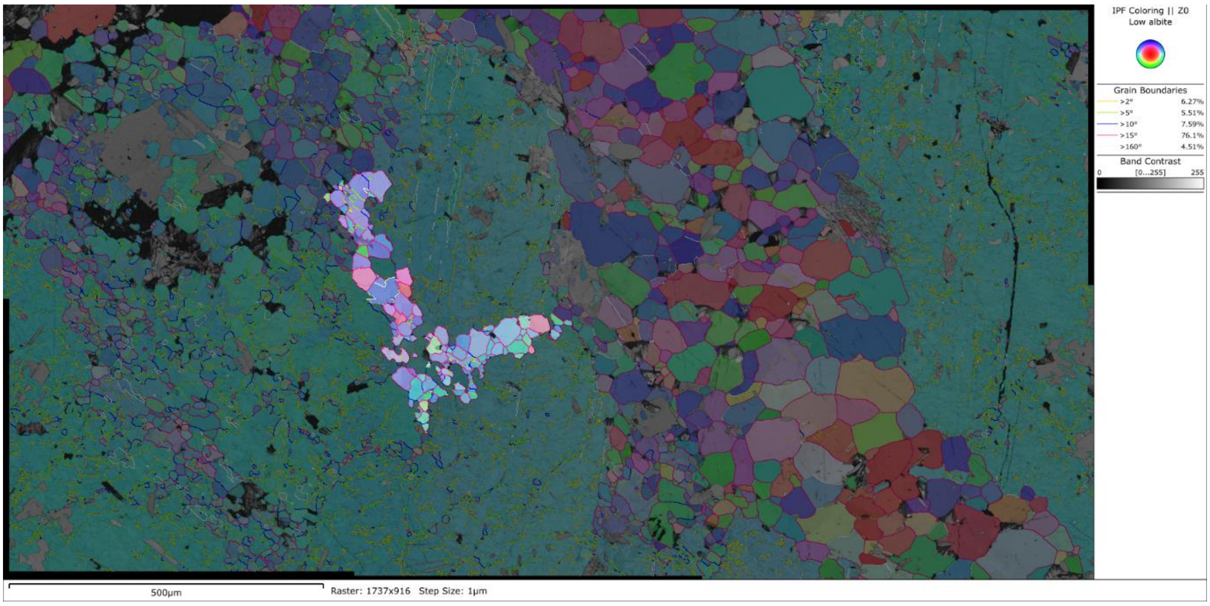

S2. Detail showing presence of [010] Burgers vectors in the dislocation population of the large albite grains.

Map showing Weighted Burgers vector directions; IPF colour scheme.

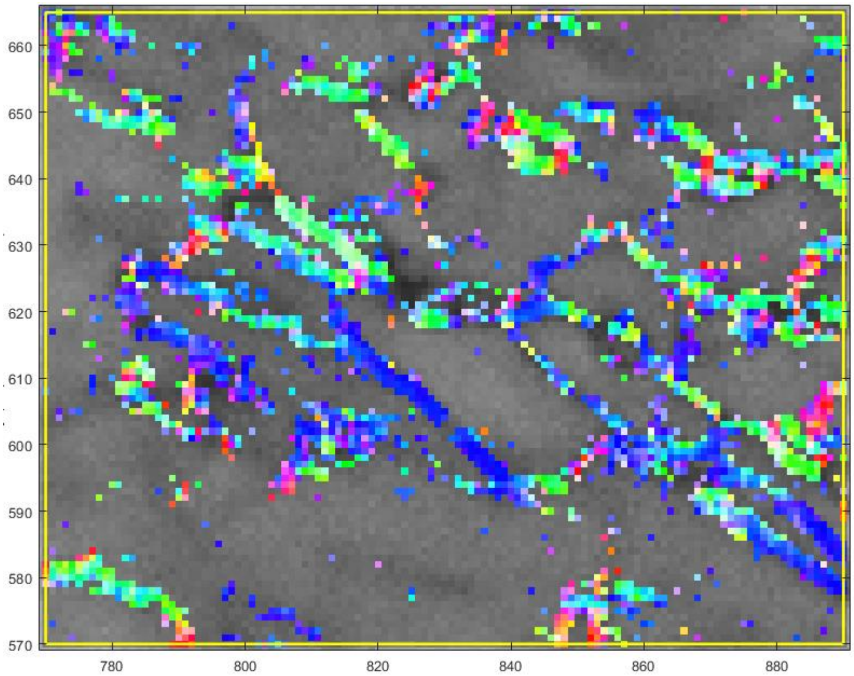

Contoured IPFs for the same map, showing a dominance of the [010] Burgers vector. Colour scale limits are the same for upper (left) and lower (right) hemispheres.

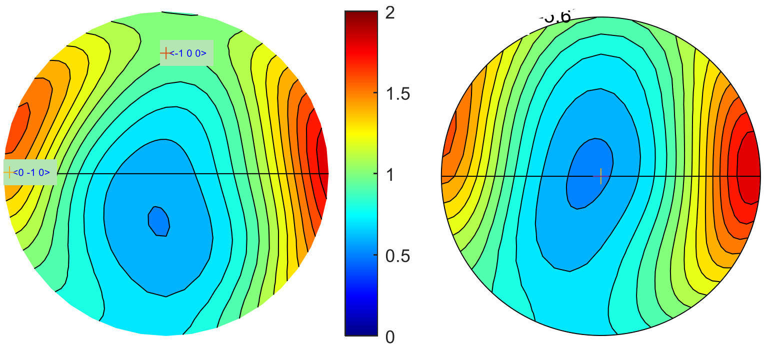

In the above map, light green lines can also be observed. These are oriented parallel to the trace of the {110} cleavage, as can be seen in the pole figures below. A diagram showing low albite crystal faces in the orientation of the grain is also shown. Red is also a common colour in the WBV direction maps, which corresponds to [001] Burgers vectors. Rows of these Burgers vectors are aligned subparallel the trace of the perfect {001} cleavage plane (see (001) pole figure below). A further subregion of the map where red and light green lines are dominant is also included below.

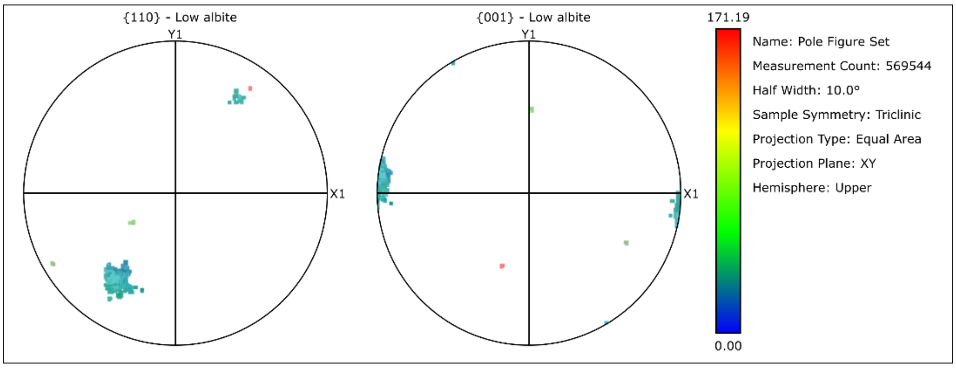

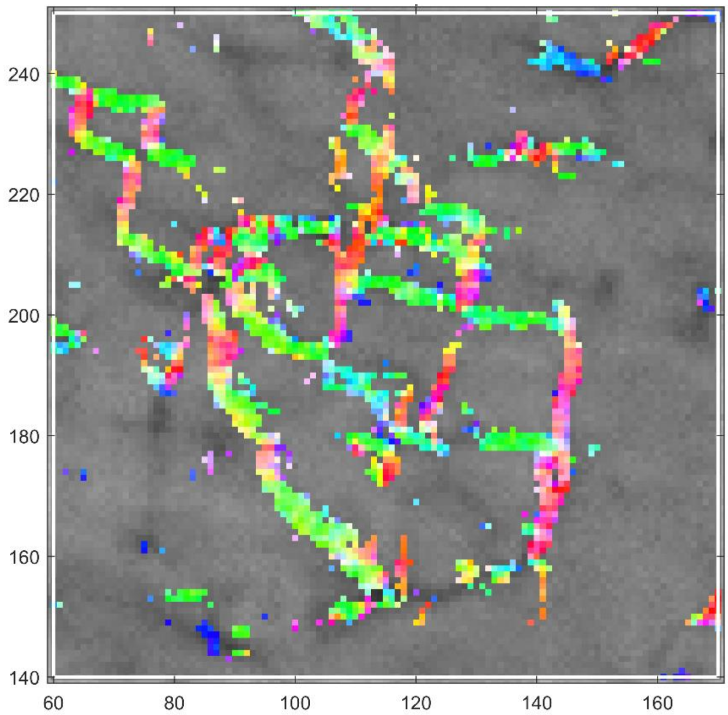

Crystal diagram:

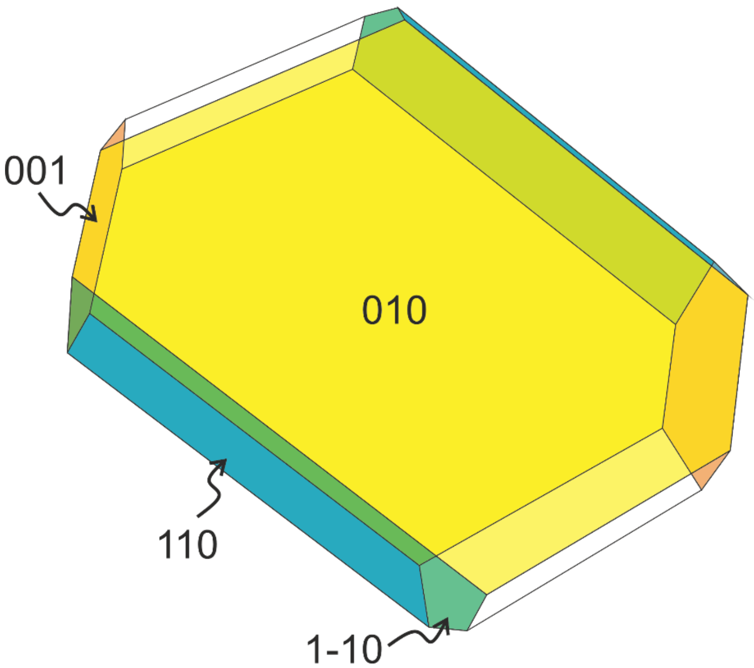

S3. Backscatter and EDX images of the twinned albite grain in Fig. 7.

Main body:

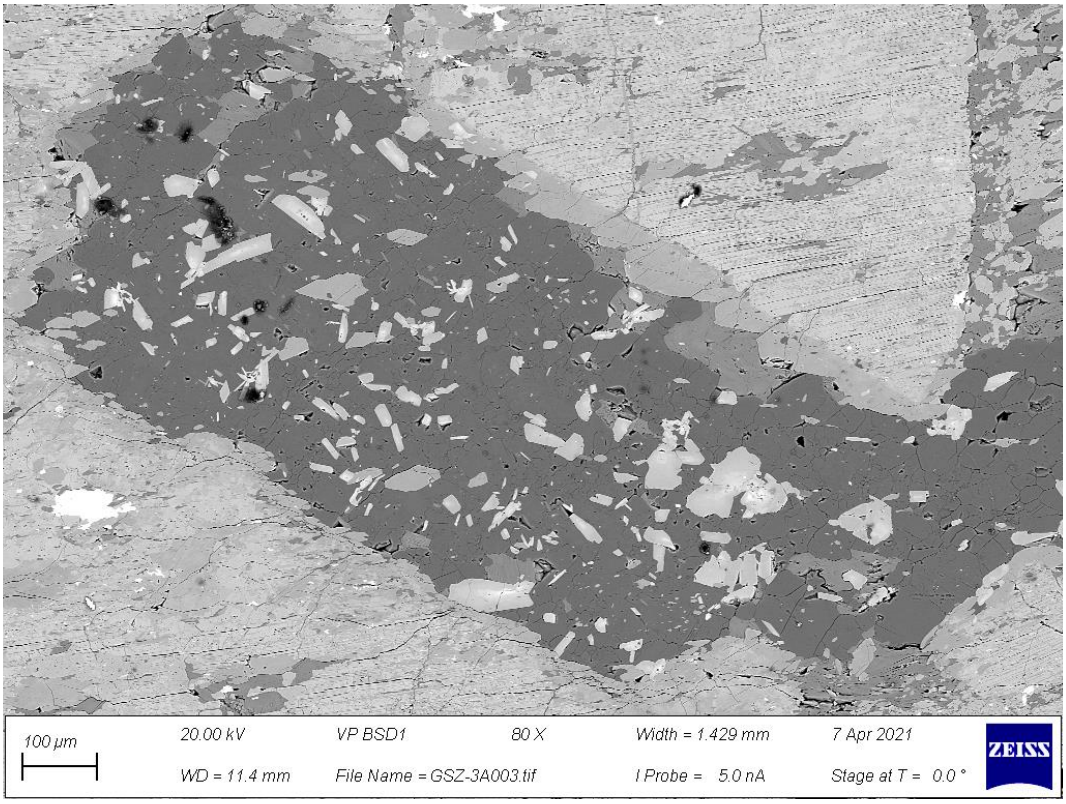

Deformed 'tail':

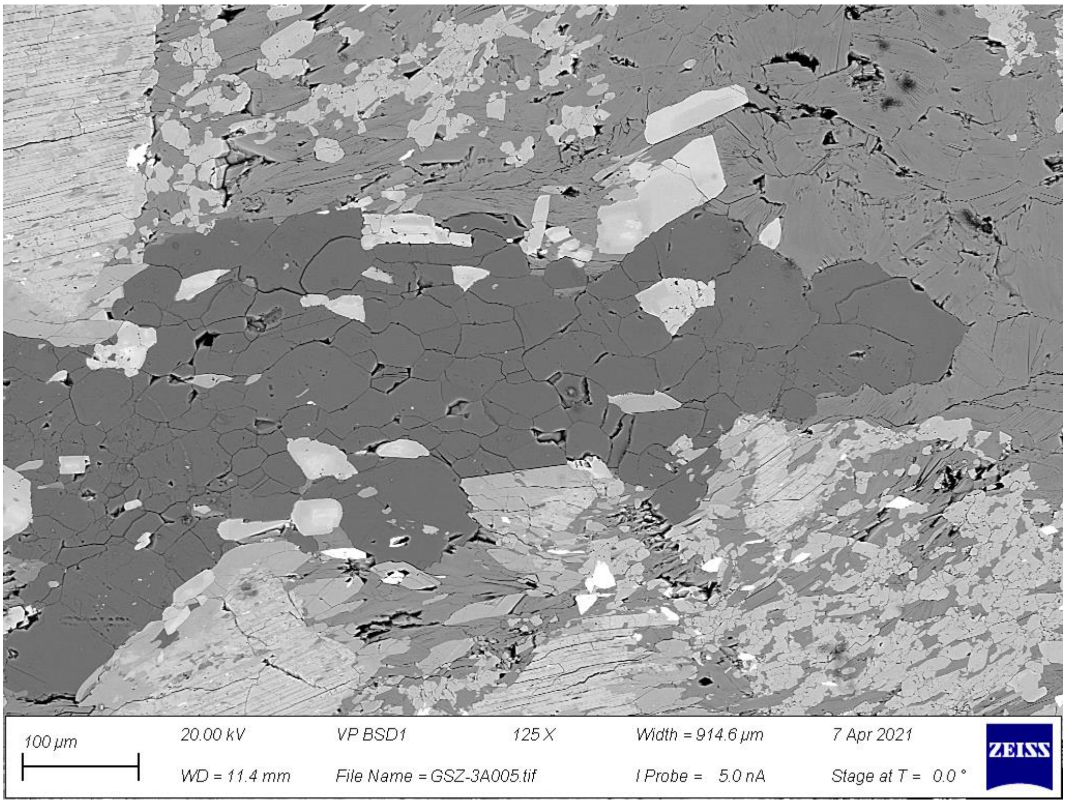

Ca:

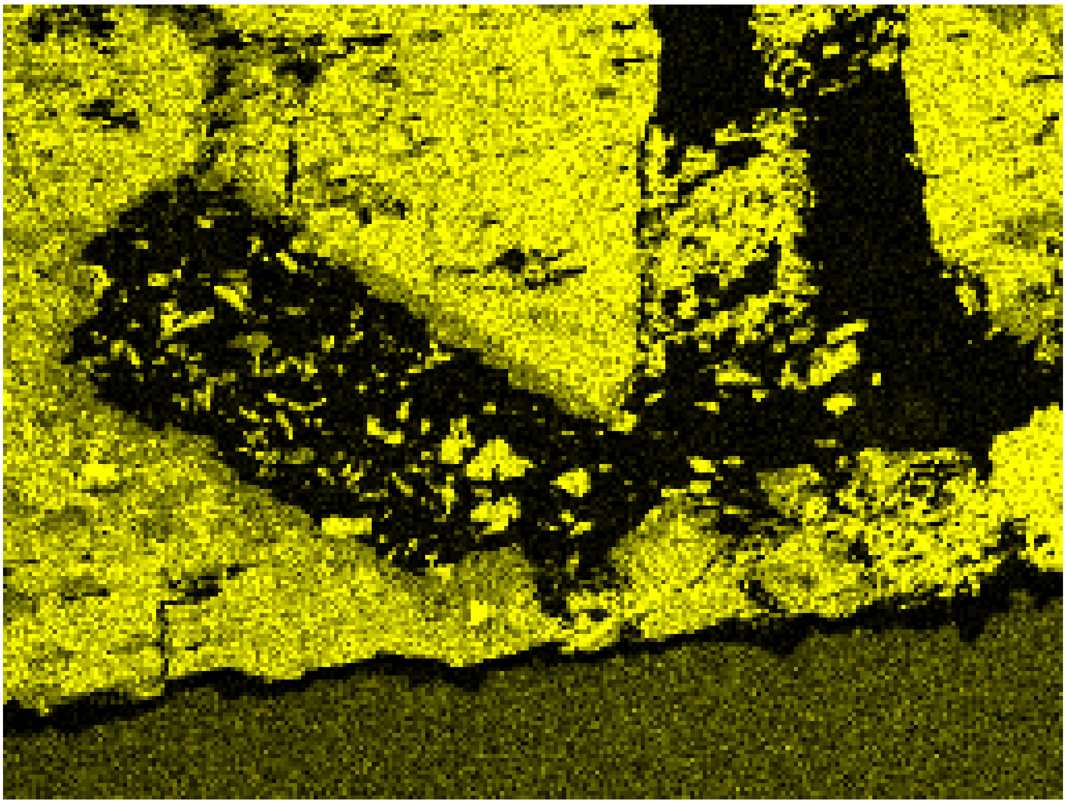

Na:

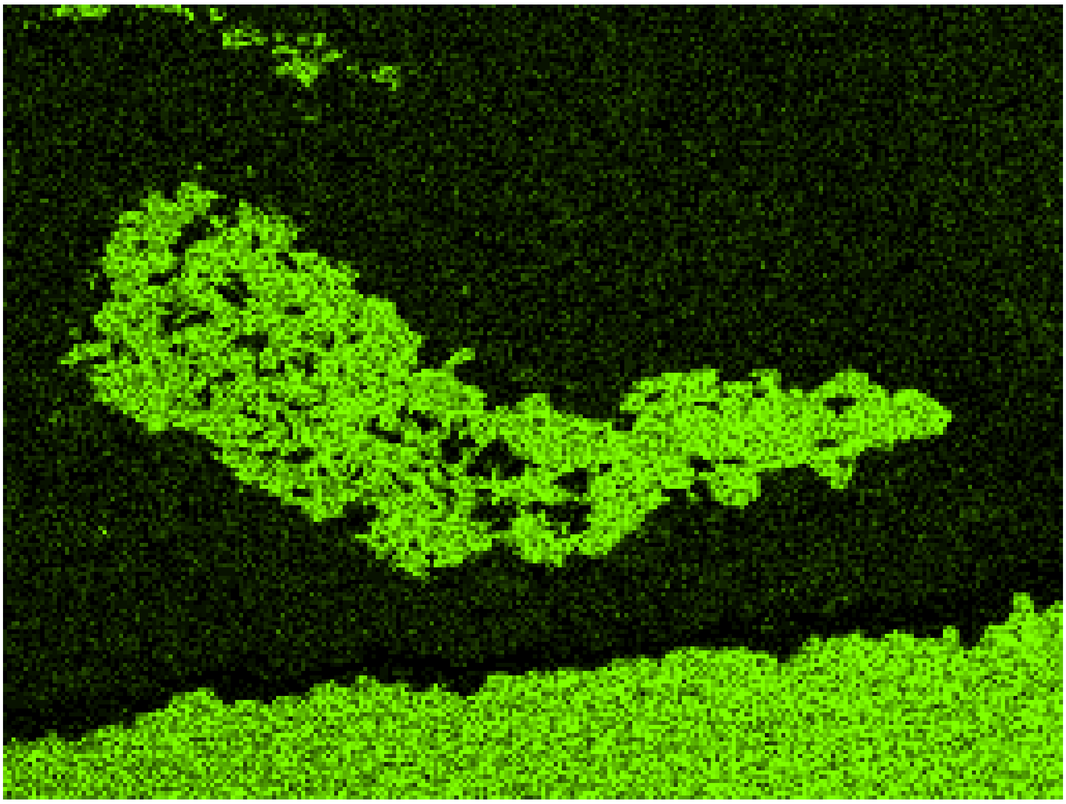

Al:

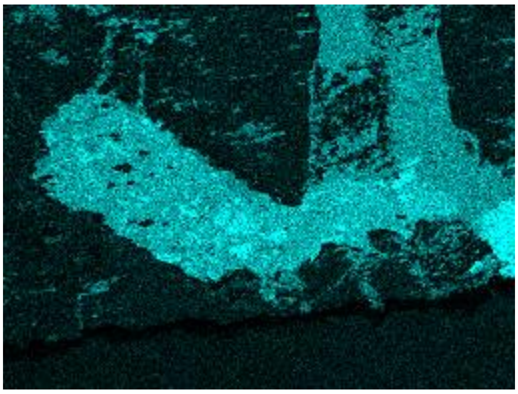

Mg:

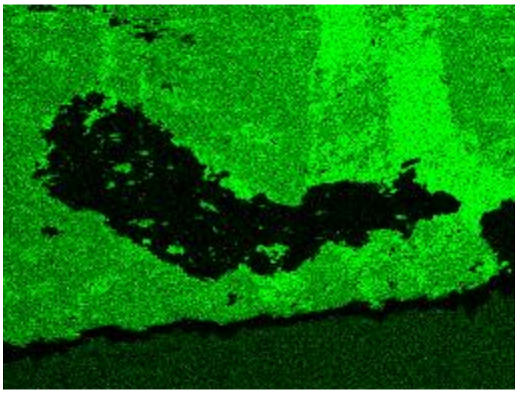

Fe:

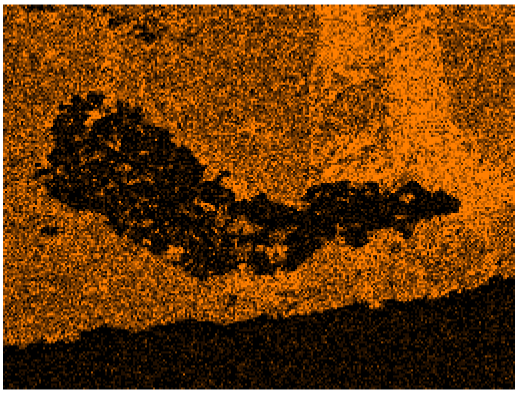

Si:

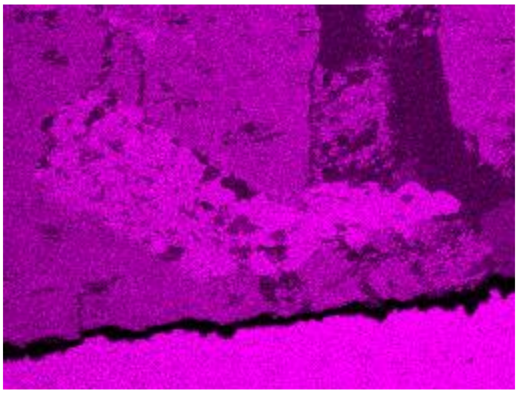

S4. Subset area and pole figures from twinned albite grain shown in Fig. 7. Colour scheme based on Euler angles. The 180° twin axis is [010] and the composition plane is sub-parallel to (001), meaning these are pericline twins.

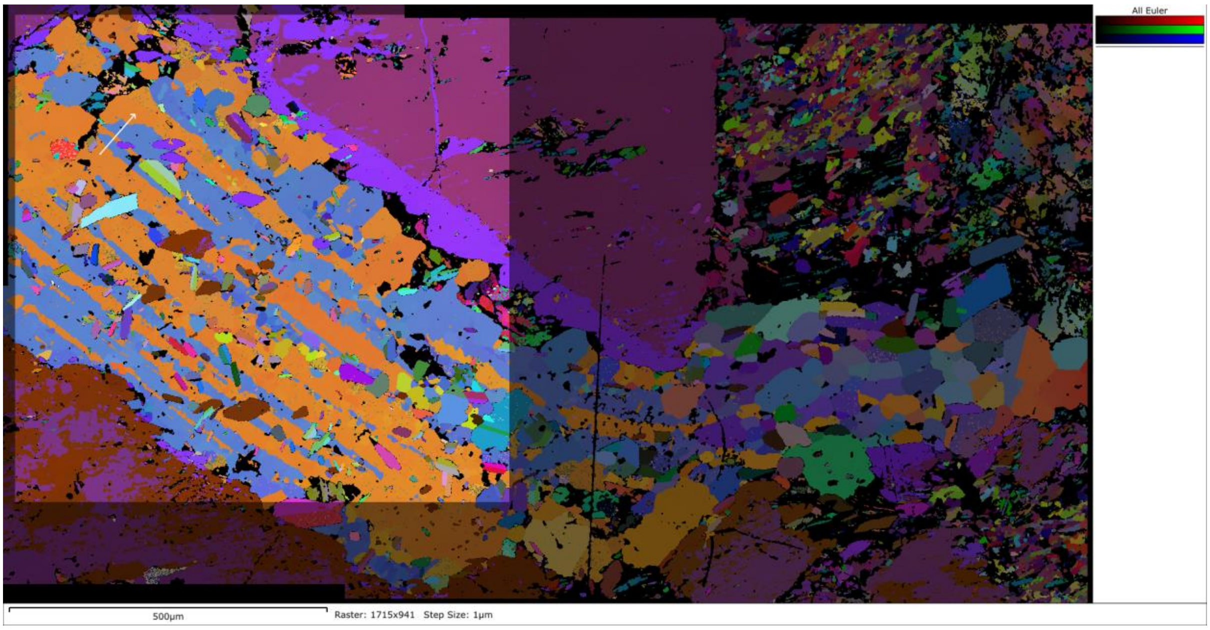

Pole figures - Upper:

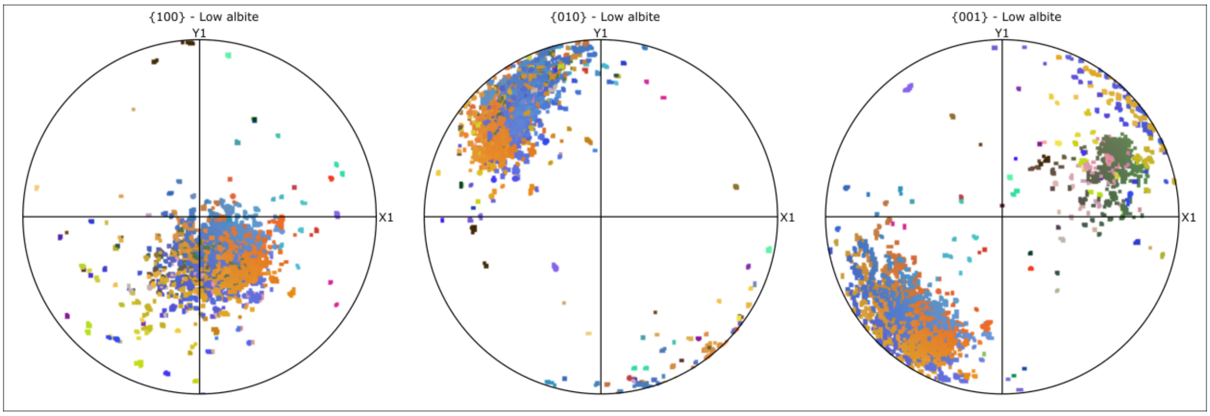

Lower:

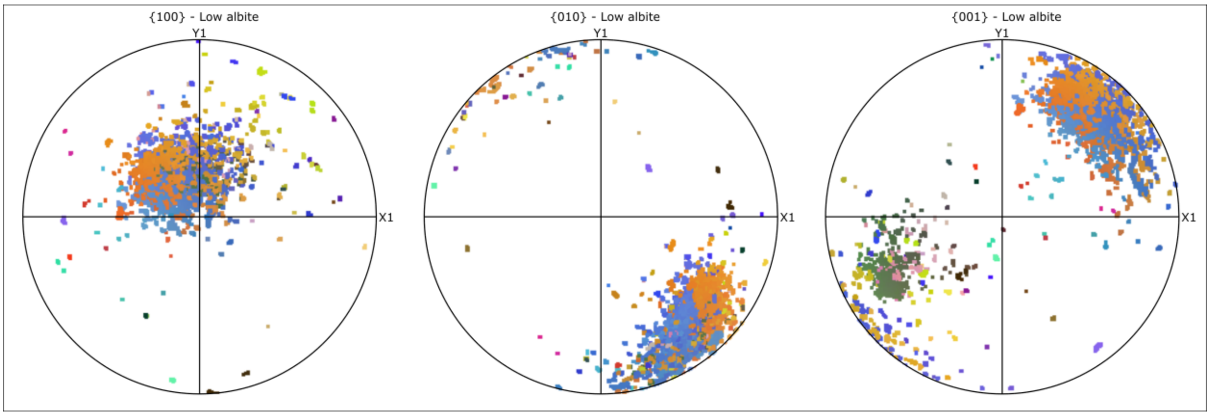

S5. Grain size distribution histograms for fine-grained bands A and B. Grain size statistics are constructed from fitted ellipse major diameter (µm) using Oxford Instruments' AZtecCrystal software. Note that EBSD produces grain sizes skewed towards small mean values. This can be influenced by the step-size used, and the presence of pixel clusters or isolated pixels.

Band A:

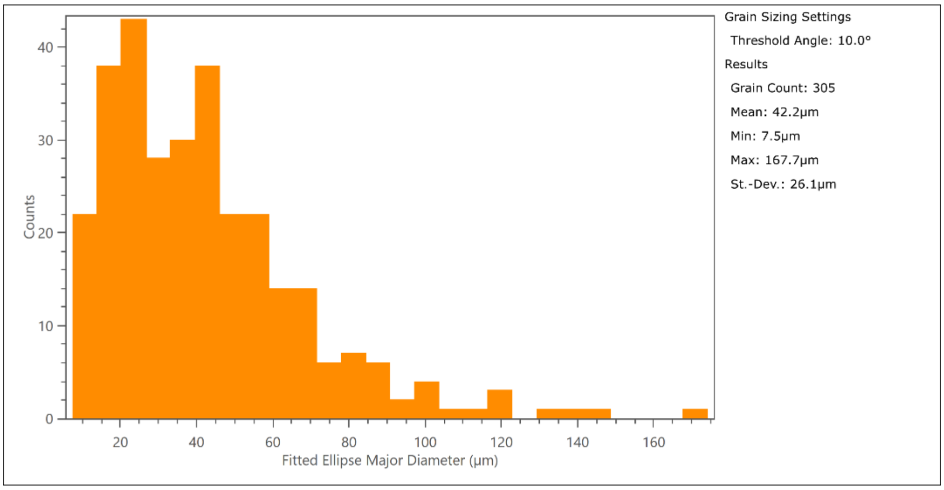

Band B: